Structural mechanisms for VMAT2 inhibition by tetrabenazine

Michael P Dalton[1], Mary Hongying Cheng[2], Ivet Bahar[2], Jonathan A Coleman[1]*

[1]Department of Structural Biology, University of Pittsburgh, Pittsburgh, United States; [2]Laufer Center for Physical and Quantitative Biology, and Department of Biochemistry and Cell Biology, School of Medicine, Stony Brook University, Stony Brook, United States

*For correspondence:
coleman1@pitt.edu

Abstract The vesicular monoamine transporter 2 (VMAT2) is a proton-dependent antiporter responsible for loading monoamine neurotransmitters into synaptic vesicles. Dysregulation of VMAT2 can lead to several neuropsychiatric disorders including Parkinson's disease and schizophrenia. Furthermore, drugs such as amphetamine and MDMA are known to act on VMAT2, exemplifying its role in the mechanisms of actions for drugs of abuse. Despite VMAT2's importance, there remains a critical lack of mechanistic understanding, largely driven by a lack of structural information. Here, we report a 3.1 Å resolution cryo-electron microscopy (cryo-EM) structure of VMAT2 complexed with tetrabenazine (TBZ), a non-competitive inhibitor used in the treatment of Huntington's chorea. We find TBZ interacts with residues in a central binding site, locking VMAT2 in an occluded conformation and providing a mechanistic basis for non-competitive inhibition. We further identify residues critical for cytosolic and lumenal gating, including a cluster of hydrophobic residues which are involved in a lumenal gating strategy. Our structure also highlights three distinct polar networks that may determine VMAT2 conformational dynamics and play a role in proton transduction. The structure elucidates mechanisms of VMAT2 inhibition and transport, providing insights into VMAT2 architecture, function, and the design of small-molecule therapeutics.

eLife assessment

The report presents the cryo-EM structure of human vesicular monoamine transporter 2 (VMAT2) bound to tetrabenazine, a clinical drug. VMAT2 is critical for neurotransmission, and the study constitutes an **important** milestone in neurotransmitter transport research. The evidence presented in the report is **convincing** and provides new opportunities for developing improved therapeutic interventions and furthering our understanding of this vital protein's function.

Introduction

Neuronal signaling by monoaminergic neurotransmitters controls all aspects of human autonomic functions and behavior, and dysregulation of this leads to many neuropsychiatric diseases. Nearly 60 years ago (*Carlsson et al., 1957*; *Kirshner, 1962*), secretory vesicles prepared from adrenal glands were shown to contain an activity that accumulated epinephrine, norepinephrine, and serotonin in an ATP-dependent manner (*Eiden and Weihe, 2011*). Extensive characterization by many different laboratories of synaptic vesicles (SVs) in neurons showed that monoamine transport activity was also dependent on the proton gradient generated by the V-ATPase, exchanging two protons for one cationic monoamine (*Henry et al., 1998*; *Eiden, 2000*; *Johnson, 1988*; *Eiden et al., 2004*; *Schuldiner et al., 1995*). Monoamine transport was shown to be inhibited by non-competitive inhibitors such as tetrabenazine (TBZ) (*Peter et al., 1994*) and competitive inhibitors like reserpine which has

been used to treat hypertension (*Eiden and Weihe, 2011*). Amphetamines were shown to be mono-amine transporter substrates, eventually leading to vesicle deacidification, disruption of dopamine (DA) packaging in the SV, and DA release into the synapse (*Freyberg et al., 2016*). Cloning of the vesicular monoamine transporter (VMAT) in the 1990s (*Liu et al., 1992*; *Peter et al., 1995*; *Erickson et al., 1992*) revealed two different genes, VMAT1 and VMAT2, that were expressed in the adrenal medulla and brain, respectively (*Peter et al., 1995*; *Weihe et al., 1994*). VMAT2 is expressed in all monoaminergic neurons in the brain, including those for serotonin, norepinephrine, DA, epinephrine, and histamine (*Eiden and Weihe, 2011*), and is essential for loading these neurotransmitters into SVs. VMAT2 is fundamentally required for neurotransmitter recycling and release (*Wang et al., 1997*; *Takahashi et al., 1997*; *Fon et al., 1997*) and changes in VMAT1 and VMAT2 activities either through small-molecule agents or mutations are thought to contribute to many human neuropsychiatric disorders including infantile-onset Parkinson's, schizophrenia, alcoholism, autism, and bipolar depression (*Lohoff et al., 2006*; *Vaht et al., 2016*; *Fehr et al., 2013*; *Bohnen et al., 2006*; *Han et al., 2020*; *Simons et al., 2013*; *Lohoff et al., 2008*).

VMAT1 and -2 are members of the solute carrier 18 (SLC18) family and are also known as SLC18A1 and SLC18A2. The SLC18 subfamily also includes the vesicular transporters for acetylcholine (*Arvidsson et al., 1997*) (VAChT, SLC18A3) and polyamines (*Hiasa et al., 2014*) (VPAT, SLC18B1). Sequence alignments also show that SLC18 transporters belong to the major facilitator superfamily (MFS) of membrane transport proteins which use an alternating access mechanism (*Jardetzky, 1966*; *Mitchell, 1957*) to transport substrate across membranes. SLC18 members are predicted to be comprised of 12 transmembrane (TM) spanning helices (TM1–12), which are arranged in two pseudosymmetric halves each with six TM helices containing a primary binding site for neurotransmitters, polyamines, and inhibitors located approximately halfway across the membrane (*Radestock and Forrest, 2011*; *Figure 1a*). Conformational changes driven by the proton electrochemical gradient are thought to alternatively expose the binding site to either side of the membrane allowing for transport of neurotransmitter from the cytoplasm to the lumen of SVs (*Yaffe et al., 2013*; *Yaffe et al., 2016*).

VMAT2 and VMAT1 share 62% sequence identity but have distinct substrate specificity and pharmacological properties (*Erickson et al., 1996*). Small-molecule ligands such as TBZ and reserpine are high-affinity inhibitors of VMAT2, which prevent neurotransmitters from binding, arrest VMAT2 from cycling, and consequently reduce neuronal signaling. VMAT2 exhibits higher affinity for TBZ, monoamines, and amphetamines, whereas reserpine binds equally to both VMAT2 and VMAT1 (*Peter et al., 1994*). TBZ is the only drug which is approved for treatment of chorea associated with Huntington's disease and has shown to be effective in various other hyperkinetic conditions such as tardive dyskinesia, dystonia, tics, and Tourette's syndrome (*Kaur et al., 2016*). A proposed mechanism for TBZ inhibition of VMAT2 involves two sequential steps, initial low-affinity binding of TBZ to the lumenal-open state of VMAT2 which produces a conformational change, resulting in a high-affinity dead-end TBZ-bound occluded complex (; *Scherman et al., 1983*; *Scherman and Henry, 1984*; *Ugolev et al., 2013*).

Here, we report a structure of VMAT2 bound to TBZ at 3.1 Å resolution in an occluded conformation using single-particle cryo-electron microscopy (cryo-EM), describing the architecture of VMAT2, identifying the high-affinity TBZ binding site, and revealing the mechanisms of drug and neurotransmitter binding, inhibition, and transport.

Results

Cryo-EM imaging of human VMAT2

Since VMAT2 is a small monomeric membrane protein of approximately 55 kDa, cryo-EM structure determination is challenging. To overcome this, we incorporated mVenus and the anti-GFP nanobody into the N- and C-terminus respectively of human VMAT2 to provide mass and molecular features to facilitate the cryo-EM reconstruction (*Figure 1b*), this created a hook-like fiducial feature by reconstituting the interaction of these proteins on the cytosolic side of VMAT2 (*Kubala et al., 2010*). Attachment of both proteins to the termini proved to be ineffective as the unstructured N- and C-terminus of VMAT2 are flexible; to combat this problem, we determined the minimal termini length that would reduce flexibility while maintaining VMAT2 folding. After successive optimizations, our final construct contained mVenus fused to the N-termini at position 17, and the anti-GFP nanobody at position 482
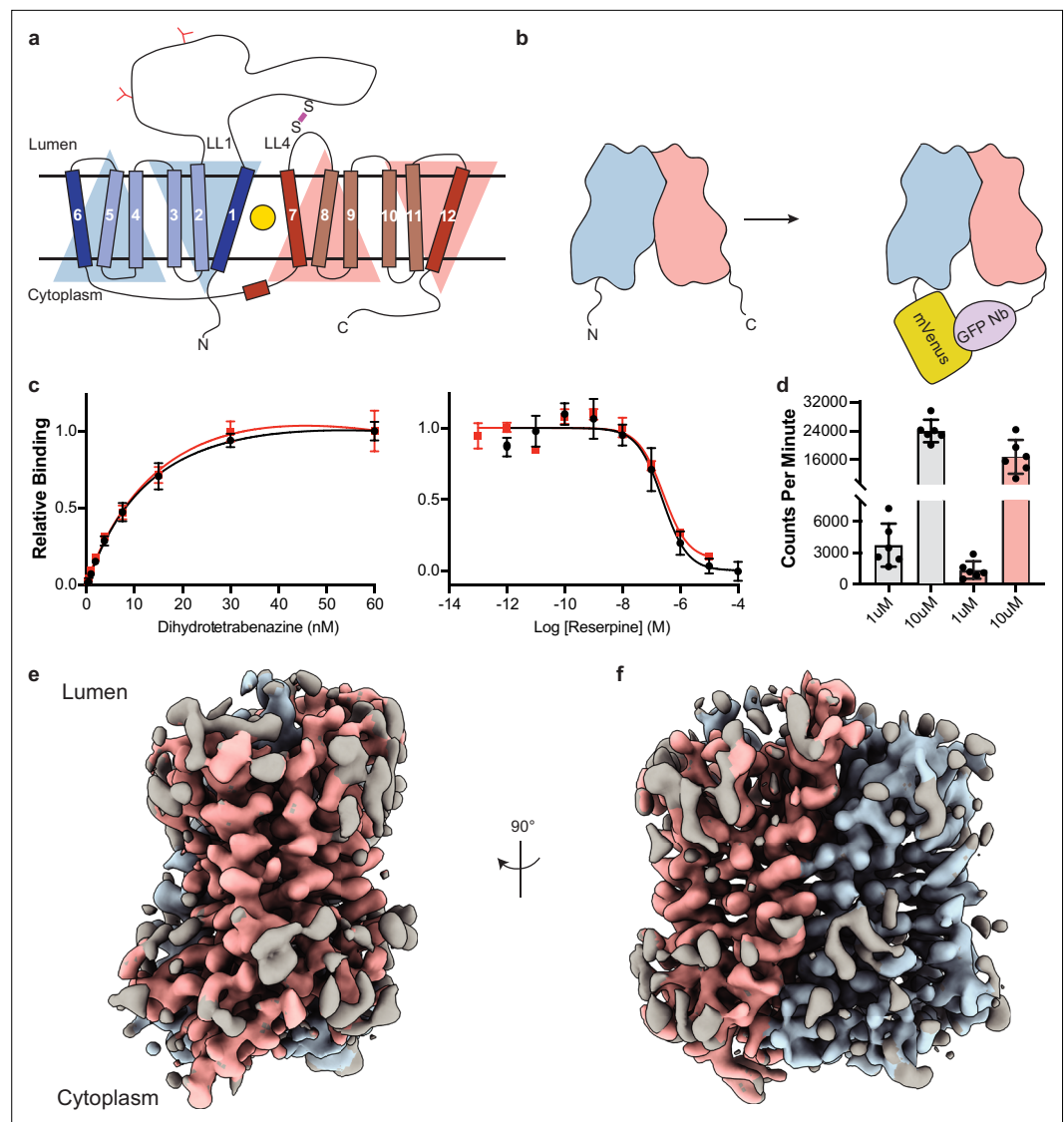
Figure 1. Cryo-electron microscopy (cryo-EM) reconstruction and functional characterization of vesicular monoamine transporter 2 (VMAT2)-tetrabenazine complex. (**a**) Predicted structural elements of VMAT2. The neurotransmitter substrate is bound at the central site (yellow, circle) between the two repeats comprised of transmembrane (TM)1–6 and 7–12. The red and blue triangles depict the pseudo twofold symmetric repeats. A disulfide bond (purple line) is predicted between lumenal loops LL1 and LL4. The N-linked glycosylation sites in LL1 are shown as red 'Y' shapes. (**b**) Intrinsic fiducial strategy involves attachment of mVenus and GFP-Nb to the N- and C-terminus of VMAT2. (**c**) Left panel, plots of [³H]-DTBZ saturation binding to wild-type VMAT2 (black, circles) and chimera (red, squares). Symbols show the mean derived from n=3 technical replicates. Error bars show the s.e.m. Right panel, graphs of competition binding of ³H-DTBZ with unlabeled reserpine, error bars show the s.e.m. DTBZ, dihydrotetrabenazine. (**d**) Plots of transport into vesicles using 1 and 10 µM ³H-serotonin for wild-type VMAT2 (gray bars) and chimera (red bars). The bars show the means and points show the value for each technical replicate. Error bars show the s.e.m. (**e, f**) Occluded map of VMAT2-tetrabenazine complex (3.1 Å resolution, contour level 0.336). The mVenus and GFP-Nb fiducial is not shown for clarity.

The online version of this article includes the following figure supplement(s) for figure 1:

Figure supplement 1. Biochemical characterization, construct design, and sequence conservation of vesicular monoamine transporter 2 (VMAT2).

Figure supplement 2. Cryo-electron microscopy (cryo-EM) data processing of the vesicular monoamine transporter 2 (VMAT2)-tetrabenazine complex.

Figure supplement 3. Cryo-electron microscopy (Cryo-EM) maps and interpretation of vesicular monoamine transporter 2 (VMAT2) reconstruction.

which we denote the VMAT2 chimera (*Figure 1—figure supplement 1a–e*). We investigated the consequences of VMAT2 modification to ensure the chimera maintained functional activity. First, we performed binding experiments with ^{3}H-labeled dihydrotetrabenazine (DTBZ) and found the chimera-bound DTBZ with a similar affinity (K_d = 26 ± 9 nM) to the wild-type control (K_d = 18 ± 4 nM) (*Figure 1c*). Competition binding of labeled DTBZ with unlabeled reserpine stabilizes cytoplasmic-open (*Yaffe et al., 2018*), a state which is incompatible with TBZ binding and produced a K_i of 173±1 nM for reserpine, which was like wild type (161±1 nM). Next, we performed transport experiments using permeabilized cells, initial time course experiments using ^{3}H-labeled serotonin showed clear accumulation (*Figure 1—figure supplement 1f*), and steady-state experiments using 1 and 10 µM serotonin measured within the linear uptake range showed similar transport activity as wild-type VMAT2 (*Figure 1d*). Thus, the functional properties of the chimera are comparable to wild-type VMAT2.

To understand the architecture, locate the drug binding site, and assess how TBZ binding influences the conformation of the transporter, we studied the VMAT2 chimera using single-particle cryo-EM (*Figure 1e and f*, *Figure 1—figure supplement 2*). The resulting cryo-EM map was determined to a resolution of 3.1 Å, the densities of the TM helices were well defined, continuous, and exhibited density features for TBZ in the primary binding site and most of the side chains (*Table 1*, *Figure 1—figure supplement 3*). This demonstrates the feasibility of our approach and enabled us to build a model of VMAT2.

Architecture of VMAT2

The TBZ-bound VMAT2 complex adopts an occluded conformation, with TBZ in a binding site between the central TM helices. The 12 TM helices of the transmembrane domain (TMD) of VMAT2 are arranged in a tight bundle with TM1–6 and TM7–12 each organized into a pseudosymmetrical half (*Figure 2a*). The cytosolic facing side of VMAT2 is characterized primarily by the unstructured N- and C- termini along with a 20-residue loop that connects the two halves, extending from TM6 to TM7 before terminating in a short α-helix that runs parallel to the bilayer and connects to TM7 with a short linker. TM5 and -11 both contain proline residues near the lumenal face, which break the helical structure and facilitate connections to TM6 and -12 respectively. TM9 and -12 exhibit significant heterogeneity in our cryo-EM reconstructions; we speculate that this is likely due to a dynamic nature intrinsic to the TMs, an aspect that may offer a glimpse into VMAT2 dynamics.

Table 1. Cryo-electron microscopy (cryo-EM) data collection, refinement, and validation statistics.

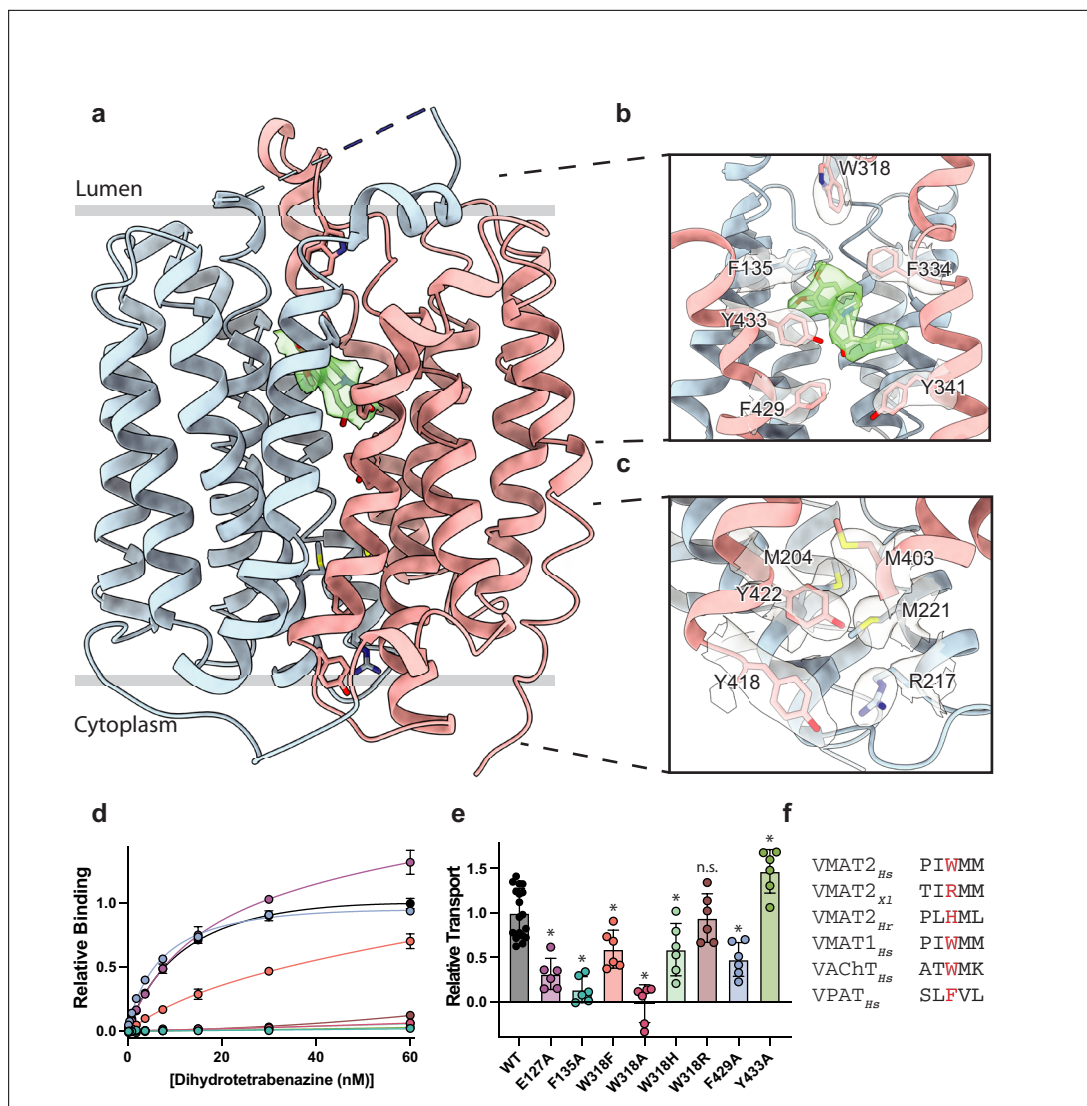|	VMAT2-TBZ (EMDB-41269) (PDB 8THR)
Data collection and processing	
Magnification	77,279
Voltage (kV)	300
Electron exposure (e⁻/Å²)	60
Defocus range (µm)	–1.0 to –2.5
Pixel size (Å)	0.647
Symmetry imposed	C1
Initial particle images (no.)	~10,000,000
Final particle images (no.)	65516
Map resolution (Å) FSC threshold	3.12 0.143
Map resolution range (Å)*	6.6–2.8
Refinement	
Initial model used (PDB code)	
Model resolution (Å) FSC threshold	3.7 0.5
Model resolution range (Å)	20.4–3.7
Map sharpening B-factor Å²	
Model composition Non-hydrogen atoms Protein residues Ligands	2937 389 1
B-factors Å² Protein Ligand	28.99 55.22
R.m.s. deviations Bond lengths (Å) Bond angles (°)	0.0004 (0) 0.37 (15)
Validation MolProbity score Clashscore Poor rotamers (%)	1.23 4.34 0.96
Ramachandran plot Favored (%) Allowed (%) Disallowed (%)	98.0 2.00 0.00

*Local resolution range at 0.5 FSC.

Figure 2. Vesicular monoamine transporter 2 (VMAT2) conformation and residues involved in gating. (**a**) Overall view of the VMAT2-tetrabenazine (TBZ) complex. TBZ is shown in light green sticks with its map density in transparent surface. (**b**) Closeup view of lumenal gating residues and TBZ, shown in stick representation together with transparent surface representation of their map density. (**c**) Cytosolic gating residues, same representation as in (**b**). (**d**) Binding of dihydrotetrabenazine (DTBZ) to various VMAT2 mutants in the lumenal and cytosolic gates including wild type (black), W318R (brown), W318H (light green), E127A (purple), W318F (orange), Y433A (forest green), F429A (blue), W318A (red), and F135A (teal). Data were normalized to wild type with error bars denoting standard deviation. (**e**) Serotonin transport activity of lumenal and cytosolic gating residue mutants. Symbols show the mean derived from n=6 technical replicates with an identical color scheme to (**d**). Asterisks denote statistical significance from wild type, with no significance being denoted with n.s. Data were normalized to wild-type transport. Statistics were calculated in GraphPad Prism using a one-way ANOVA with Dunnett's multiple comparison test. Error bars show the standard deviation. (**f**) Alignment of five sequential residues of human VMAT2 (two residues on either side of W318) against their counterparts in *Xenopus laevis* (*Xl*), *Helobdella robusta* (*Hr*), and VMAT1, VAChT, and VPAT from humans. The residues which align with W318 in VMAT2 are shown in red.

The online version of this article includes the following figure supplement(s) for figure 2:

Figure supplement 1. Sequence alignment of vesicular monoamine transporter 1 (VMAT1), VMAT2, VAChT, and VPAT.

VMAT1 and -2 encode a large lumenal loop (LL) 1 which contains several N-linked glycosylation sites (*Yao and Hersh, 2007*) and a disulfide bridge between LL1 and LL4 (*Thiriot et al., 2002*). LL1 and -4 also contain intriguing elements of structure: LL1 extends into the lumenal space in an unstructured loop which is mostly not resolved in our structure, before terminating in a short helix which interacts with the lumenal face of the transporter near TM7, -11, and -12; LL4 extends outward from TM7 into the lumen before connecting back to TM8. A striking feature of LL4 is the location of W318

which positions its indole side chain directly into a lumenal cavity near the TBZ site, acting as a plug to completely occlude the lumenal side of the transporter (*Figure 2b*). Together, these loops cinch the lumenal side of the transporter closed, locking VMAT2 in an occluded conformation and preventing ligand egress. The conserved nature of LL4 and W318 suggests this motif is necessary for transport function and is a key player in the transport mechanism (*Figure 1—figure supplement 1b and g*, *Figure 2—figure supplement 1*). The conformation of LL1 and -4 is also likely aided by a disulfide bond between cysteines 117 and 324, which is known to be necessary for transporter function (*Thiriot et al., 2002*), our structure was not able to unequivocally place this bond due to the lack of density for residues 48–118 of LL1.

Cytosolic and lumenal gates

The structure of the VMAT2-TBZ complex reveals that both the cytosolic and lumenal gates are closed, which precludes solvent and ligand access from either the cytosolic or lumenal compartments (*Figure 2a–c*). Previous studies have suggested that residues R217, M221, Y418, and Y422 make up the cytosolic gate (*Yaffe et al., 2016*). We find R217 and Y418 form the outer cytosolic gate with the guanidino group of R217 involved in a cation-π interaction with the aromatic benzyl group of Y418 which seals off cytosolic access to the binding site (*Figure 2c*). M221 and Y422 form a second set of cytosolic gating residues 'above' the outer cytoplasmic gate through a stable methionine-aromatic interaction which acts to fully seal the cytoplasmic gate (*Figure 2c*). It is likely that M204 and M403 also contribute to cytosolic gating in this region as their side chains also act to fill this space. On the lumenal side, F135, F334, and W318 form the lumenal gate where they interact with one another to block access to the binding site. W318 acts as 'cap' with the indole side chain facing into a tightly packed hydrophobic pocket consisting of residues I44, V131, L134, L315, I317, and I381 which completely prevent access on the lumenal side. W318 is highly conserved in the SLC18 family, suggesting that SLC18 transporters share a common mechanism of lumenal-gate closure (*Figure 2—figure supplement 1*). E127 of LL1 may play a role in stabilizing the tryptophan in this conformation, with the carboxyl group of the side chain orienting itself near the indole nitrogen potentially forming a hydrogen bond pair. We found that mutation of this residue to alanine did not significantly reduce TBZ binding relative to wild type (*Figure 2d*). The inner gate is located just below TBZ and comprises residues Y341, F429, and Y433 (*Figure 2b*; *Yaffe et al., 2016*). When probed for their role in inhibitor

Table 2. Calculated K_d values of dihydrotetrabenazine (DTBZ) for various single-point mutants.

Mutant	K_d (nM)
WT	15±3
N34A	ND
N34D	ND
N34Q	ND
N34T	ND
E127A	15±6
F135A	ND
R189A	ND
V232L	ND
E312Q	ND
W318A	ND
W318F	24±16
W318H	ND
W318R	ND
F429A	7.7±0.6
Y433A	ND

binding, we found that alanine mutants of F135, Y433, and W318 all greatly reduced DTBZ binding (*Figure 2d*). Extensive contacts of TBZ with F135 may function to keep the transporter closed on the lumenal side, which would trap VMAT2 in the occluded conformation. F135 and Y433 form π-stacking interactions with TBZ which coordinate the benzene ring of TBZ. F429A did not reduce DTBZ affinity (K_d = 7.7 ± 0.6 nM) compared to the wild-type control (K_d = 15 ± 2 nM), showing that while mutation of this residue compromises the inner cytosolic gate (*Figure 2b*), it is not directly involved in binding TBZ. Conversely, while W318 in LL4 also does not interact directly with TBZ, W318 is required for stabilizing the occluded conformation, and replacement with alanine prevents TBZ from being trapped inside the transporter by preventing closure of the lumenal gate. Sequence alignment with other members of the SLC18 family reveals broad conservation of W318 except for VAChT which contains a phenylalanine in its place (*Figure 2—figure supplement 1*) and a W318F mutation retained some DTBZ binding (K_d = 24 ± 16 nM) (*Table 2*, *Figure 2d*). Alignment of VMAT2 sequences from other species also shows a high degree of conservation of W318 with some notable exceptions which substitute W318 for a large positively charged residue such as an arginine or histidine; and upon investigation we found these mutants all greatly diminish DTBZ binding (*Figure 2d*).

To further investigate the functional role of the identified gating residues, we performed serotonin transport experiments. We found that mutation of both E127 and F135 to alanine significantly reduced transport activity (*Figure 2e*). E127A produced a large reduction in transport, resulting in just 34% activity. Replacing F429 with alanine reduced transport as well, but only to about half the level of wild type (*Figure 2e*). Interestingly, the Y433A mutation appeared to enhance transport, and while critical for TBZ binding, this mutant does not prevent transporter cycling (*Figure 2d and e*). Mutation of W318 to alanine greatly reduced transport, paralleling the effect observed with DTBZ binding
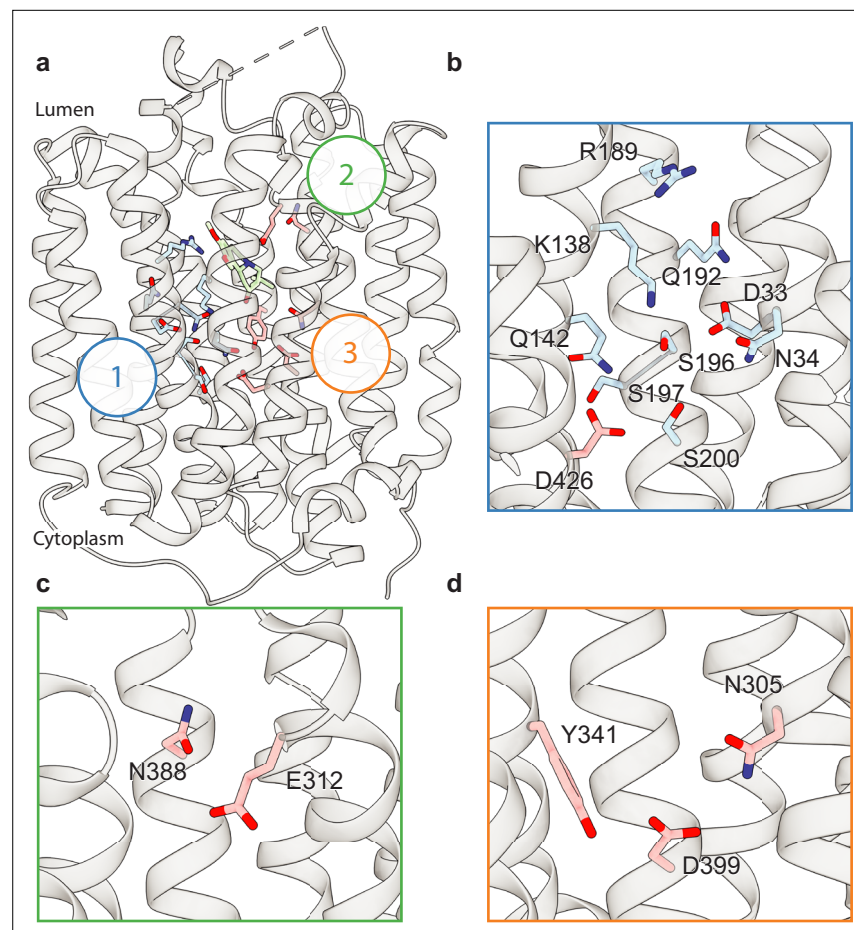

Figure 3. Polar networks. (**a**) Overall view showing three distinct polar networks. Polar residues involved in each network and tetrabenazine (TBZ) are shown in sticks. (**b**) Cartoon representation showing a zoomed view of polar network 1. (**c**) Polar network 2. (**d**) Polar network 3.

(*Figure 2d and e*) while a histidine mutant at this position maintained a significant amount of transport activity (*Figure 2d–f*) and the phenylalanine substitution had about half the activity of wild type. The highest activity of the examined W318 mutants was W318R, which fully recapitulated the transport activity of wild type despite being unable to bind DTBZ (*Figure 2d and e*).

Polar networks

Upon careful inspection of the model, we were able to identify distinct polar networks that we believe may play a role in proton coordination and subsequent transporter conformational change (*Figure 3a*). The first and largest of these networks lies between TM-1, -4, and -11, and consists of residues D33, N34, K138, Q142, R189, Q192, S196, S197, S200, and D426 (*Figure 3b*; *Yaffe et al., 2013*). At the center of this network lies D33 (*Yaffe et al., 2013*), which makes critical contacts with the side chains of N34, K138, S196, and Q192. Together, the residues comprise a complex hydrogen bond network linking TM1, -4, and -11. D426 (*Merickel et al., 1997*) lies further toward the cytosol with the side chain carboxyl group facing the bulk of the network, likely forming a hydrogen bond with the hydroxyl group of S200. In the other TMD half there are two distinct groups of interacting polar residues, which bridge between TM7, -8, and -10 (*Figure 3a, c, and d*). The second group is a pair of residues found on the lumenal side, between residues E312 and N388 with the amide group of the N388 side chain pointed toward the carboxyl group of E312, which could act to stabilize TBZ in the binding site (*Figure 3c*). The third group is located toward the cytosolic side and consists of N305, Y341, and D399 (*Merickel et al., 1997*), the latter two of which have previously been speculated to form a hydrogen bond pair (*Yaffe et al., 2013*). The side chains of these residues are positioned toward one another, with the carboxyl group of D399 forming a hydrogen bond with N305 and likely Y314 (*Figure 3d*).

TBZ binding site

The resolution of our map allowed us to unambiguously place TBZ in the central binding site (*Figure 4a and b*). TBZ adopts a pose which is predominantly perpendicular to the direction of the TM helices in the lumenal half of VMAT2 near the location of the lumenal gating residues. The TBZ binding site exhibits an amphipathic environment, comprised of both polar and non-polar residues where the tertiary amine of TBZ orients itself toward the negatively charged surface of the binding site near TM7 and -11, and toward E312 (*Figure 4c*, *Figure 4—figure supplement 1a*). We considered that E312 may play an analogous role to the highly conserved aspartate residue present in neurotransmitter sodium symporters such as the serotonin, DA, and norepinephrine transporters (*Yamashita et al., 2005*) which utilize a negatively charged residue to directly bind to amine groups (*Figure 4d and e*, *Figure 2—figure supplement 1*). We thus performed radiolabeled binding experiments to assess the effect of mutating residues in the TBZ binding site by measuring binding of ^{3}H-labeled DTBZ (*Figure 4f*, *Table 2*). E312 was previously shown to be necessary for substrate transport and inhibitor binding, so we first selected this residue for mutagenesis to probe its importance in TBZ binding (*Yaffe et al., 2013*; *Støve et al., 2022*). The E312Q mutant did not fully abolish DTBZ binding (*Figure 4—figure supplement 1b*) but did greatly reduce DTBZ affinity. This demonstrates that, while not completely essential, E312 is important for inhibitor binding and likely substrates transport by interacting with the amine of the neurotransmitter (*Figure 4d and e*). Next, we observed that R189 orients its guanidino group toward the methoxy groups of TBZ likely forming hydrogen-bonding interactions and we found that replacement of R189 with an alanine nearly completely abolished DBTZ binding at all concentrations tested (*Figure 4f*, *Figure 4—figure supplement 1b*). The high degree of conservation of this residue suggests that it plays an important role in transporter function, and even a conservative substitution to a lysine nearly eliminated DTBZ binding (*Figure 4f*, *Table 2*). K138 has been previously shown to play an important role in both TBZ binding and serotonin transport and the primary amine side chain is positioned toward the TBZ binding site (*Merickel et al., 1997*; *Figure 4d and e*). K138 is positioned between two aspartate residues (D426 and D33) and is part of a hydrogen bond network that has been previously hypothesized (*Merickel et al., 1997*). Previous experiments found that mutating K138 to alanine resulted in an approximate fourfold reduction in TBZ binding affinity (*Yaffe et al., 2013*) but did not extinguish TBZ binding and therefore K138 is likely involved in direct interactions with substrate or inducing conformational changes during proton transport and is not directly involved in TBZ binding. N34 is of particular interest since the amide group of its side chain appears to form a hydrogen bond with the carbonyl oxygen of TBZ (*Figure 4d and e*) which
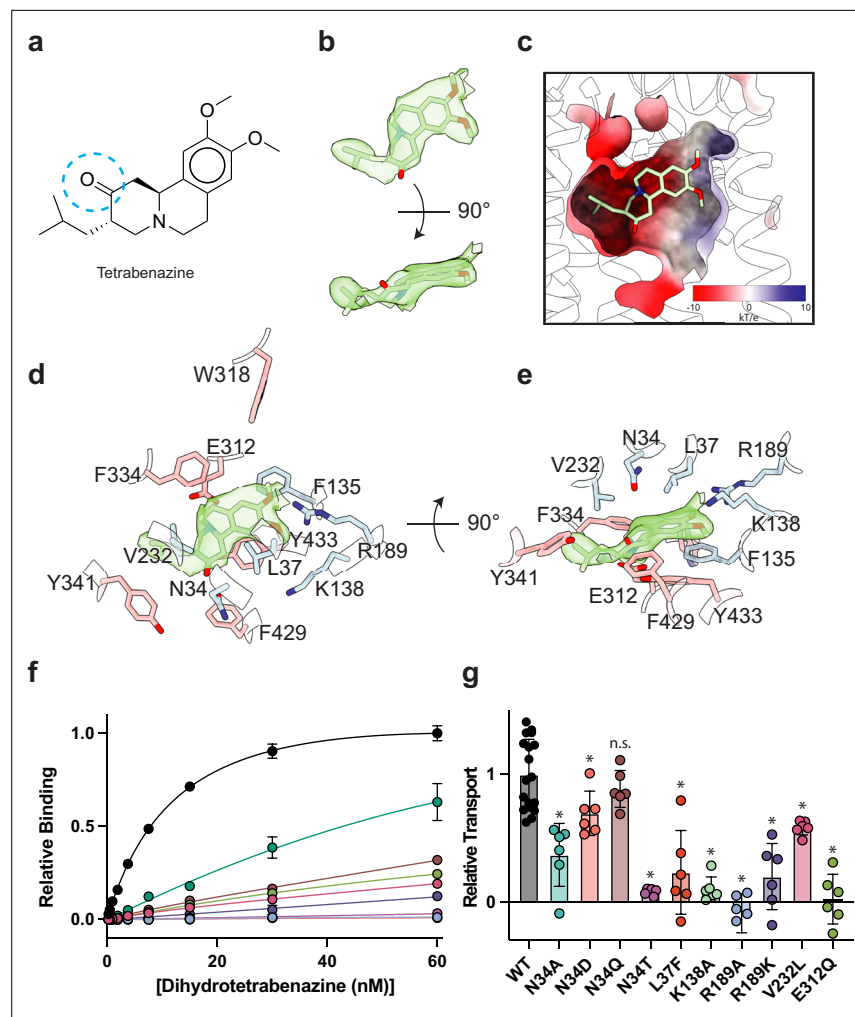
Figure 4. Tetrabenazine (TBZ) recognition and binding. (**a**) Chemical structure of TBZ. The blue dotted circle indicates the position of the hydroxyl group in dihydrotetrabenazine (DTBZ). (**b**) Density associated with TBZ is shown in green transparent surface sharpened with a B-factor of –50 Å². TBZ is shown in sticks fit to the density. (**c**) Electrostatic potential of the TBZ binding site. (**d, e**) Binding site of TBZ, residues which are involved in binding are shown in sticks. Density associated with TBZ is shown in light green surface. (**f**) Plots of ³H-DTBZ saturation binding to wild type (black), V232L (pink), R189A (blue), E312Q (forest green), N34D (orange), N34T (light purple), N34A (teal), N34Q (brown) R189K (purple) L37F (red), and K138A (light green). (**g**) Serotonin transport activity of mutants in TBZ binding site. Symbols show the mean derived from n=6 technical replicates with an identical color scheme to f. Asterisks denote statistical significance from wild type, with no significance being denoted with n.s. Statistics were calculated in GraphPad Prism using a one-way ANOVA with Dunnett's multiple comparison test. Error bars show the s.e.m.

The online version of this article includes the following video and figure supplement(s) for figure 4:

Figure supplement 1. Point mutants in tetrabenazine (TBZ) binding site.

Figure supplement 2. Tetrabenazine (TBZ) docking and molecular dynamics (MD) simulations.

Figure supplement 3. Effects of protonation states of tetrabenazine (TBZ) and selected vesicular monoamine transporter 2 (VMAT2) residues on the time evolution of TBZ (heavy atoms) and VMAT2 (α-carbons) root-mean-square-deviations (RMSDs) from their original (cryo-electron microscopy [cryo-EM]-resolved) positions.

Figure 4—video 1. Binding and coordination of neutral tetrabenazine (TBZ) (cyan van der Waals [vdW] representation) observed in a 180 ns molecular dynamics (MD) simulation (run 1).
https://elifesciences.org/articles/91973/figures#fig4video1

Figure 4—video 2. Binding and coordination of neutral tetrabenazine (TBZ) (cyan van der Waals [vdW] representation) observed in a 180 ns molecular dynamics (MD) simulation (TBZ_1 run 2), in the same format as

Figure 4 continued on next page

Figure 4 continued

Figure 4—video 1.
https://elifesciences.org/articles/91973/figures#fig4video2

Figure 4—video 3. Binding and coordination of neutral tetrabenazine (TBZ) (cyan van der Waals [vdW] format) observed in a 180 ns molecular dynamics (MD) simulation (TBZ_1 run 3), in the same format as *Figure 4—video 1*.
https://elifesciences.org/articles/91973/figures#fig4video3

---

is a hydroxyl group in DTBZ. DTBZ binding was not detectable to N34 mutants of either glutamine, threonine, or aspartate while substitution to alanine preserved some binding (*Figure 4f*, *Table 2*, *Figure 4—figure supplement 1b*).

To investigate the functional role of residues in the binding site, we again performed a series of serotonin transport experiments. We found R189A, E312Q, N34T, N34A, and K138A mutations all exhibited reduced transport activity (*Figure 4g*). R189A and E312Q exhibited the largest change, reducing transport to essentially zero. Substitution of N34 with glutamine had little or no effect on transport activity, opposite of what was noted for DTBZ binding. Replacing N34 with alanine was detrimental, reducing transport to less than half of wild type (*Figure 4g*). We found N34D and N34T to have opposing effects, with N34D having activity slightly less than wild type and N34T having little to no transport activity at all. R189K greatly affected transport but retained some activity despite lacking measurable DTBZ binding.

Our model of the VMAT2-TBZ complex allowed us to pinpoint two residues which contribute to the specificity of TBZ to VMAT2 over VMAT1. Previous studies have highlighted V232 (*Støve et al., 2022*), which is a leucine in VMAT1, as being putatively involved in conferring differences in affinity, and our model shows that V232 is positioned closely to the isobutyl of TBZ which is wedged into a small hydrophobic pocket (*Figure 4—figure supplement 1*). The addition of an extra carbon of the leucine side chain would produce a steric clash and limit the ability of TBZ to bind (*Figure 4e*). The V232L mutant in VMAT2 reduces the affinity of DTBZ to VMAT2, confirming its importance in specificity, but the V232L mutant did not show a complete loss in binding (*Figure 4f*, *Figure 4—figure supplement 1b*). Therefore, we carefully inspected the binding site of VMAT2 and compared it to the predicted structure of VMAT1 to find additional differences in the binding site (*Figure 2—figure supplement 1*), we found that L37 in VMAT2 is a phenylalanine in VMAT1 (*Figure 4—figure supplement 1c*). Given its proximity

to TBZ, this substitution would produce a steric clash with the benzene ring (*Figure 4—figure supplement 1a and c*). We found that the L37F mutant resulted in nearly no detectable binding of DTBZ at 60 nM concentration (Figure 4-figure supplement 4b). Thus, the combination of these two substitutions likely constitutes the differences in TBZ affinity of VMAT2 vs. VMAT1. Interestingly, V232L and L37F both retained some transport activity with L37F producing a more significant reduction in activity (*Figure 4g*).

Our docking simulations suggested that TBZ may sample two different binding poses by small reorientation and movements within the same binding pocket (*Figure 4—figure supplement 2*), both exhibiting similar binding affinities (–9.5±0.2 kcal/mol); the first pose is almost identical to that resolved in our cryo-EM structure (0.4 Å root-mean-square-deviation [RMSD], *Figure 4—figure supplement 2e*); and the second (3 Å RMSD in TBZ heavy atom coordinates) shows a reorientation of the TBZ methoxy groups toward C430, a residue previously identified to play an important role in binding TBZ (*Thiriot and Ruoho, 2001*; *Figure 4—figure supplement 2f*). These two
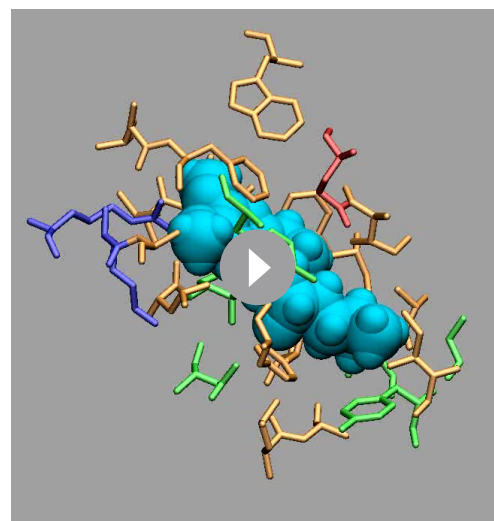

Video 1. Same as *Figure 4—videos 1–3*, with neutral tetrabenazine (TBZ), but with the additional protonation of D426 (TBZ_3 run 1).(Related to *Table 3*). TBZ adopted the predominant pose similar to that resolved in the cryo-electron microscopy (cryo-EM) structure.

https://elifesciences.org/articles/91973/figures#video1
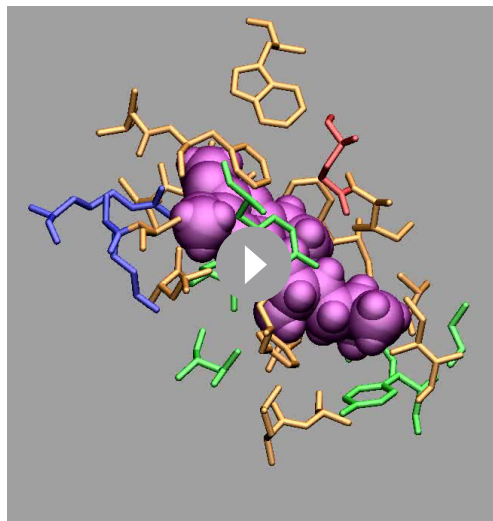
Video 2. Molecular dynamics (MD) simulation of the binding and coordination of protonated tetrabenazine (TBZ) (TBZ$^+$; *pink* van der Waals [vdW] format) to vesicular monoamine transporter 2 (VMAT2) with protonated E312 and D399. (Related to *Table 3*). This is a 100 ns run, termed TBZ_2 run 1. The same format as *Figure 4—videos 1–3* is adopted for the coordinating residues. TBZ tends to alter its binding pose to approximate the one observed in *Figure 4—video 2*.
https://elifesciences.org/articles/91973/figures#video2
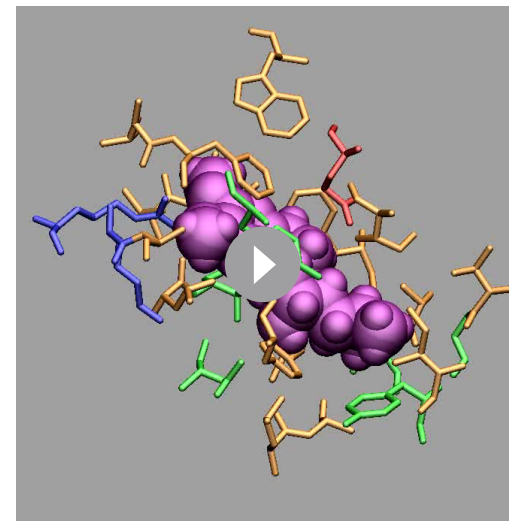
Video 3. Same as *Video 1*, except for the protonation of tetrabenazine (TBZ) (TBZ$^+$ shown in pink van der Waals [vdW] representation). (Related to *Table 3*).This is a 100 ns run, termed TBZ_4 run 1. In the presence of protonation, TBZ preferentially samples the pose observed in *Figure 4—video 2*, *Video 2*.
https://elifesciences.org/articles/91973/figures#video3

poses were also observed in molecular dynamics (MD) simulations as illustrated in *Figure 4—figure supplement 2a–d* and *Figure 4—videos 1–3*, *Video 1*. The second pose provides insights into the adaptability of TBZ to the conformational dynamics of VMAT2, while it preferentially positions itself into the pocket resolved in our cryo-EM map. TBZ is thought to enter from the lumenal side of VMAT2 by binding to the lumenal-open conformation (*Ugolev et al., 2013*). It may interact first with C430 and the other coordinating residues at this pose before R189 moves between the two methoxy groups and allows TBZ to settle into the resolved orientation (*Figure 4—figure supplement 2f*). This result highlights the stepwise events that inhibitors like TBZ may undergo to stably bind to their targets.

The binding stability of TBZ is also influenced by its protonation state. When TBZ is protonated (TBZ$^+$), it induces the diffusion of three to four times more water molecules within the TBZ binding pocket compared to neutral TBZ (*Table 3*, *Figure 4—figure supplement 3*). This flux of water results in the dissociation of TBZ from its binding site as illustrated in *Videos 2 and 3*. Several titratable residues, including D33, E312, D399, D426, K138, and R189, line the central cavity of VMAT2 and impact TBZ binding stability (*Table 4*). We found that maintaining an overall neutral charge within the TBZ binding pocket, as observed in system TBZ_1, most effectively preserves the TBZ-bound occluded state of VMAT2. Residues R189 and E312 in particular are within close proximity of TBZ and participate directly in binding.

Neurotransmitter release

To examine the binding propensity of DA to VMAT2 in the occluded conformation, we constructed five simulation systems with varying protonation states for the four acidic residues (D33, E312, D399, and D426) that line the binding pocket (*Table 5*). For all five systems, DA carried a +1 charge and was initially placed with a pose predicted by docking simulations to be the most favorable binding pose (*Figure 5—figure supplement 1a and b*); and for each system, two MD runs of 100 ns were performed, except for the case where all acidic residues were in a protonated state of which one of the runs was extended to 200 ns to visualize the release of DA to the vesicular lumen. The simulations revealed alterations in DA's binding properties depending on the protonation states of the four acidic

Table 3. Molecular dynamics (MD) simulation systems of vesicular monoamine transporter 2 (VMAT2) in the presence of tetrabenazine (TBZ), their properties and simulation durations.

System ID	Protonated residues	Bound ligand	Duration (ns)	Waters in binding pocket*	RMSD in VMAT2 Cα-atoms (Å)†	RMSD in TBZ heavy atoms (Å) ‡
TBZ_1		TBZ	3×180	2.8±1.3	2.4±0.3	2.7±0.5
TBZ_2	E312 and D399	TBZ$^+$	2×100	8.1±1.4	2.4±0.4	5.9±1.4
TBZ_3	E312, D399, and D426	TBZ	3×100	4.6±1.4	2.7±0.5	3.5±1.3
TBZ_4		TBZ$^+$	2×100	14.3±2.4	2.3±0.2	3.7±0.4

*Number of water molecules within 3.5 Å of TBZ (or TBZ$^+$) averaged over multiple MD snapshots.
†RMSDs (root-mean-square-deviations) of VMAT2 Cα-atoms from their initial (cryo-EM resolved) positions.
‡RMSD of the heavy atoms of TBZ from their cryo-EM-resolved positions. All averages and standard deviations were calculated between 50 and 100 ns portion of the MD trajectories.

residues (*Figure 5—figure supplement 1c*, *Table 5*). Two notable differences were observed when comparing DA to TBZ binding (system DA_2 vs. TBZ_1). First, upon binding TBZ, R189 orients its guanidino group toward the methoxy groups of TBZ and forms hydrogen bonds in both the cryo-EM structure and MD simulations; in the case of DA, hydrogen bond formation of the hydroxyl groups

Table 4. pK_a calculations performed by PROPKA 3.5.0.

Residue	pK_a with TBZ	pK_a without TBZ	Model pK_a
D33	5.48	5.43	3.8
D121	4.46	4.46	3.8
D123	4.75	4.75	3.8
D213	3.23	3.23	3.8
D214	4.95	4.95	3.8
D262	6.44	6.44	3.8
D291	4.44	4.44	3.8
D399	7.64	7.56	3.8
D411	2.74	2.74	3.8
D426	6.38	6.35	3.8
D460	8.19	8.07	3.8
E120	3.06	3.06	4.5
E127	4.77	4.77	4.5
E215	4.27	4.27	4.5
E216	3.91	3.91	4.5
E244	4.52	4.52	4.5
E278	4.22	4.22	4.5
E312	6.71	7.46	4.5
E321	4.53	4.53	4.5
K138	9.86	10.04	10.5
R189	9.10	10.02	12.5
TBZ	8.57		10

The cryo-EM structure (with or without TBZ) was used for pK_a calculations using PROPKA 3.5.0. Key residues of interest are written in boldface.

Table 5. Molecular dynamics (MD) simulations of vesicular monoamine transporter 2 (VMAT2) in the presence of dopamine and the observed events.

System #	Protonated residues	Duration (ns)	Waters in binding pocket*	VMAT2 RMSD[†] from cryo-EM (Å)	Observed events
DA_0	None	2×100	7.7±1.5	2.6±0.2	Salt bridge formation between DA and D399; influx of water into the binding pocket.
DA_1	D399	2×100	10.5±2.2	2.2±0.2	Salt bridges formation between DA and E312; influx of water into the binding pocket.
DA_2	E312, D399	2×100	8.8±2.1	2.2±0.3	Fluctuations in DA binding pose while remaining within the binding pocket. Formation of two water wires.
DA_3	E312, D399, D426	2×100	8.8±2.1	2.5±0.2	Fluctuations in DA binding pose; dislocation of DA from its binding site in one of the two simulations.
DA_4	E312, D399, D426, D33	1×100 1×200	11.7±2.3	2.6±0.3	Fluctuations in DA binding pose; dislocation and release of DA in the 200 ns run.

*Number of water molecules within 3.5 Å of dopamine averaged over MD snapshots recorded in the time interval 50–100 ns.

[†]RMSDs (root-mean-square-deviations) in VMAT2 C^α-atoms positions; all averages and standard deviations refer to the portion 50–100 ns of MD simulations.

of DA was primarily facilitated by K138, D33 or D426, or N34, rather than R189. This resulted in the exposure of R189, triggering a continuous water pathway near the hydrophobic gate residue F135 (*Figure 5a*). This water path recurred in multiple runs conducted with DA and was lined by the hydrophilic network composed of Y182, R189, Q192, S137, K138, D33, N34, Q142, N146, S200, and D426 (*Figure 5—figure supplement 1d*).

Second, an additional water wire near the hydrophobic gate residue F334 was observed in DA-bound VMAT2 (*Figure 5a*), but not in TBZ-bound VMAT2 which, in contrast, was minimally hydrated (*Figure 5b*). The second water wire was lined by the backbone polar groups of hydrophobic residues, e.g., F334, together with a hydrophilic network containing K379, N388, S338, E312, Y433, Y341, N305, and D399. We also observed that the amine group of DA acted to facilitate the water influx from the lumenal side.

We hypothesize that those two water paths may be related to proton transfer and be associated with protonating the pocket-lining acidic residues. Likely, lumenal DA release depends on the number of protonated acidic residues (*Figure 5—figure supplement 1d–h*). When at least two acidic residues were protonated, we observed fluctuations in DA position (run DA_2; *Video 4*) and dislocation of DA from its pocket (run DA_3; *Video 5*). In system DA_4 (*Table 5*), the protonation of E312, D399, D426, and D33 resulted in complete opening of the hydrophobic gates formed by F135, W318, and F334, which led to the release of DA to the vesicle lumen (*Figure 5c*, *Figure 5—video 1*). DA was observed to migrate toward a cluster of acidic residues, including E127, E120, D121, and D123, before complete dissociation, and the acidic environment within the vesicle lumen should assist in promoting the release of DA.
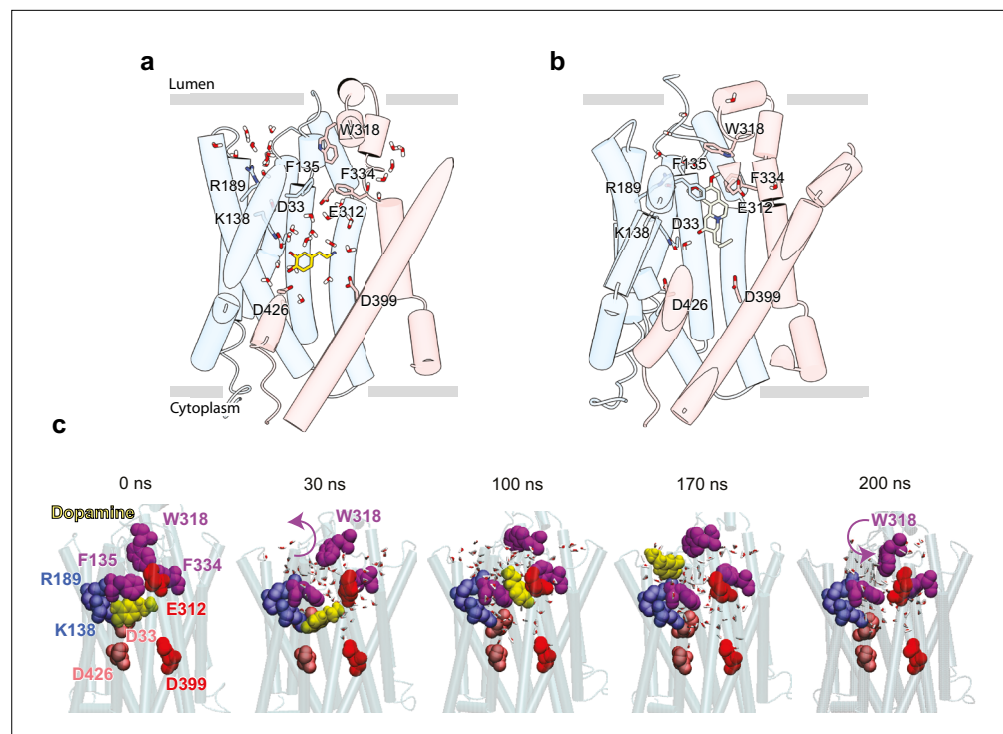
Figure 5. Release of dopamine (DA) from the occluded binding site to the lumen through the lumen-facing vestibule and concurrent conformational changes in vesicular monoamine transporter 2 (VMAT2). Comparison of (**a**) DA (*yellow* sticks) and (**b**) tetrabenazine (TBZ) (green sticks) binding to VMAT2, captured by molecular dynamics (MD) simulations. Two water pathways are observed in the MD simulations of VMAT2 bound to DA (run DA_2 in *Table 5*). Water molecules and key residues are shown in sticks. (**c**) Positions of DA (*yellow* van der Waals [VDW] spheres) with respect to hydrophobic gate composed of F135, W318, and F334 (*purple* VDW spheres), and charged residues lining the binding pocket at t=0, 30, 100, 170, and 200 ns. W318 side chain isomerization plays a critical role in mediating the opening/closure of the hydrophobic gate, accompanied by the reorientation of F135 side chain, permitting a flux of water molecules eventually giving rise to the destabilization and release of DA to the synaptic vesicle (SV) lumen by translocating through a hydrated channel. Waters within 10 Å radius from the center of mass (COM) of the hydrophobic gate residues are displayed.

The online version of this article includes the following video and figure supplement(s) for figure 5:

Figure supplement 1. Comparisons of binding poses of substrate (dopamine [DA] and serotonin) and inhibitor (tetrabenazine [TBZ]) from docking simulations and molecular dynamics (MD) simulations under different protonation states of substrate-coordinating and/or gating residues.

Figure 5—video 1. Release of dopamine (DA) to the vesicular lumen (yellow van der Waals [VDW] spheres), observed after protonating D33, E312, D399, and D426 (red vdW spheres). Related to *Figure 5*.
https://elifesciences.org/articles/91973/figures#fig5video1

Discussion

The VMAT2-TBZ complex captures the transporter in a fully occluded state with the ligand binding site centrally located between the two repeated substructures TM1–6 and TM7–12. VMAT2 functions by alternating access which involves alternate exposure of the primary binding site to either side of the membrane and isomerization between a cytosolic-open and lumenal-open state in a mechanism known as the rocker-switch (*Figure 6a and b*; *Eiden and Weihe, 2011*; *Radestock and Forrest, 2011*; *Drew et al., 2021*). Studies have proposed that TBZ first enters VMAT2 from the lumenal side, binding to a lumenal-open conformation (*Scherman et al., 1983*). TBZ makes extensive contact with residues in the primary site, likely in a lower affinity state as the transporter subsequently closes to forming the high-affinity occluded state. The lumenal gates lock the transporter into an occluded state, preventing displacement by other ligands and producing a so-called dead-end complex (*Yaffe et al., 2016*; *Kaur et al., 2016*; *Scherman et al., 1983*; *Chen et al., 2012*; *Figure 6a*).
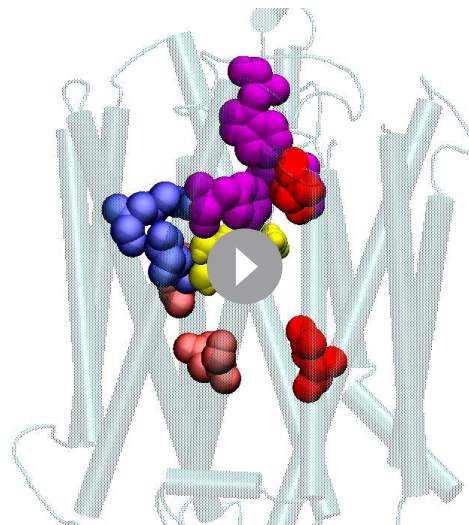
Video 4. Fluctuations in dopamine binding pose (DA; *yellow* van der Waals [vdW] spheres) within its binding pocket, observed in a 100 ns molecular dynamics (MD) simulation of vesicular monoamine transporter 2 (VMAT2) in the presence of DA (system DA_2 in *Table 5*). Related to *Table 5*. VMAT2 E312 and D399 are protonated; and D33 and D426 are deprotonated. Hydrophobic gate residues F135, W318, and F334 are displayed in *purple* vdW spheres, and acidic and basic residues K138 and R189 are shown in *red* and *blue* vdW representation.

https://elifesciences.org/articles/91973/figures#video4
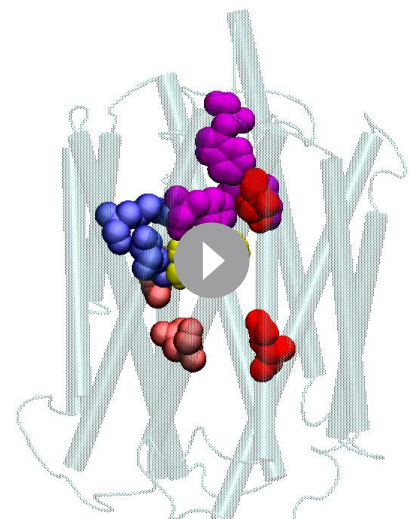
Video 5. Release of dopamine (DA; yellow van der Waals [vdW] spheres) from the binding pocket, observed in a 100 ns molecular dynamics (MD) simulation (system DA_3 in *Table 4*). (Related to *Table 5*). E312, D399, and D426 were protonated and D33 was deprotonated.

https://elifesciences.org/articles/91973/figures#video5

Comparison of the TMD with more distantly related MFS transporters in other conformational states such as the outward-open VGLUT2 (*Li et al., 2020*) and inward-open GLUT4 (*Yuan et al., 2022*) models (1.2 Å RMSD) shows that the conformational changes involving TM1, -7, -8, and -11 are likely involved in mediating the transport cycle and alternating access (*Figure 6—figure supplement 1*). Comparison with the AlphaFold model shows that while the TMD is largely similar (1.1 Å RMSD overall difference in TMD), AlphaFold lacks several key features such as the conformations of the LLs and is unable to predict key details that are critical to ligand binding. Hence, computational docking could not identify the TBZ binding site using the AlphaFold-predicted model, alluding to the critical importance of our experimental structural data (and simulations based on that structure) for gaining insights into VMAT2 functional mechanisms.

To enable us to solve the structure of VMAT2, we developed an intrinsic fiducial tool consisting of mVenus and the anti-GFP Nb which provides a feature on the cytosolic side of the transporter. GFP and the GFP-Nb are ubiquitous tools used for cell biology, protein biochemistry, and structural biology and here we describe another application of this powerful toolkit. In contrast to traditional antibody-based campaigns which may require multiple rounds of screening and take many months or years to discover a suitable binder, our strategy only required us to make between 15 and 20 constructs to find a suitable chimera (*Figure 1—figure supplement 1a–c*). There are now many other similar methods such as the fusion of the target protein with BRIL and binding of the anti-BRIL Fab (*Mukherjee et al., 2020*) and fusions of maltose-binding protein and DARPin (*Chen et al., 2023*). However, since our strategy directly incorporates fluorescent proteins, this enables FSEC-based screening of constructs and monitoring fluorescence throughout purification (*Hattori et al., 2012*). One obvious disadvantage of all intrinsic fiducial strategies is that the fusion may distort the protein structure, but monitoring the functional activity and comparison with the wild-type protein should mitigate these problems.

Among human mutations in VMAT2 causing an infantile-onset form of parkinsonism (*Jacobsen et al., 2016*; *Rilstone et al., 2013*; *Padmakumar et al., 2019*), three mutants, P316A, P237H, and P387L, have been shown to extinguish monoamine transport. We find these residues are in LL4 and the lumenal ends of TM5 and -9, respectively (*Figure 6—figure supplement 2*). LL4 is involved in lumenal gating and the P316A variant would likely disrupt the conformation of the loop. In the case of P237H, a histidine would result in not only an insertion of a positively charged residue into the lumenal
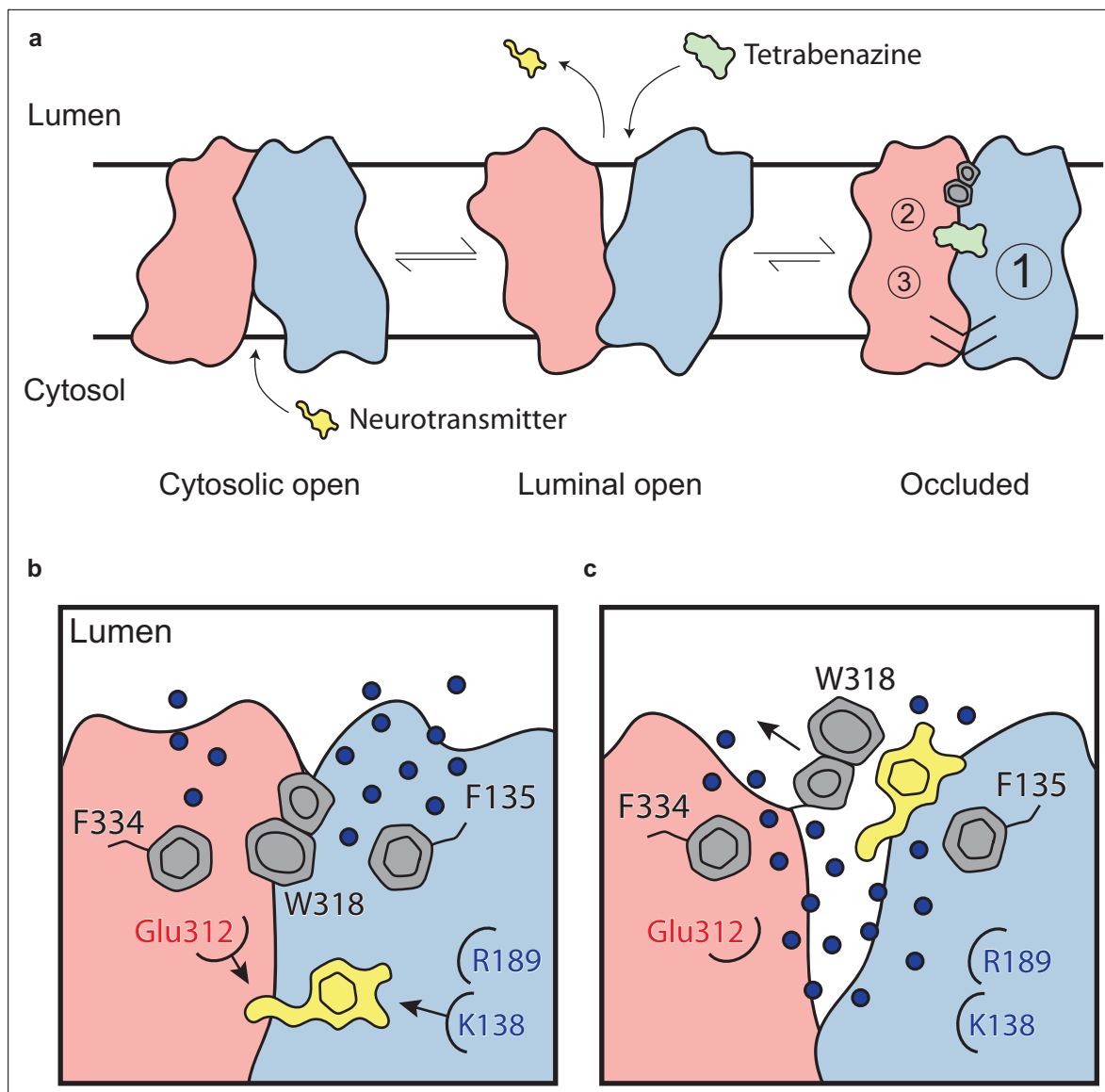
Figure 6. Mechanism of tetrabenazine inhibition, and the roles of gating residues and polar interactions networks. (**a**) Cartoon depicting substrate transport and tetrabenazine binding to vesicular monoamine transporter 2 (VMAT2). Neurotransmitter (yellow cartoon) binds to the cytosolic-open conformation before being released from the transporter in the lumenal-open state. Tetrabenazine (green cartoon) binds to the lumenal-facing state and induces a conformational change to a high-affinity occluded conformation which is the resolved cryo-electron microscopy (cryo-EM) structure reported in this work. The VMAT2–tetrabenazine complex highlighting significant features including both cytosolic (slashes) and lumenal gates (hexagon and pentagon depicting W318), the three polar networks (numbered circles) and relative location of the tetrabenazine binding site (green). (**b**) Water penetrating through two pathways is involved in opening the lumenal gate. Dopamine is shown in yellow cartoon. (**c**) Opening of W318 is associated with neurotransmitter release.

The online version of this article includes the following figure supplement(s) for figure 6:

Figure supplement 1. Comparison of the vesicular monoamine transporter 2 (VMAT2)-tetrabenazine (TBZ) structure with the predicted AlphaFold structure and with other major facilitator superfamily (MFS) transporters.

Figure supplement 2. Human variants of vesicular monoamine transporter 2 (VMAT2).

membrane interface but also in a reduction of the helical bend and would distort the connection of TM5 with TM6. The P387L variant would also disrupt helical connections and the overall architecture of the helix by insertion of a bulky residue into a small hydrophobic cavity. Therefore, we speculate that these SNPs alter the transporter's ability to sample multiple conformations by suppressing transporter dynamics and perturbing VMAT2 stability and folding. Recently, many additional disease

variants have been discovered (*Saida et al., 2023*), many of which are also found in the lumenal or cytoplasmic ends of TM helices, LL1, and the N- and C-termini, and our structure will provide insight into the functional and structural consequences of these variants.

Large aromatic side chains of the lumenal gating residues compartmentalize the transporter, likely ensuring directional transport of substrate. MD simulations revealed little variation in the pose of the aromatic gating residues comprising the inner gates (*Figure 4—figure supplement 2d*). It is interesting to note that substitution of Y433 with alanine resulted in enhanced transport while reducing DTBZ binding. Reduced inhibitor binding is likely due to disruption of π-stacking interactions, but the mechanism for enhanced transport remains unclear. The lumenal gates showed more movement in MD simulations of DA, likely owing to its residue composition and lack of strong interactions (*Figure 5*). Despite this observation, we assert that the tight hydrophobic environment prevents exchange into the lumenal space. These mechanisms of gating are atypical of MFS transporters which more commonly use salt bridges to gate access to the substrate binding site (*Drew et al., 2021*).

Of particular interest among gating residues is W318, which acts as a central plug to prevent solvent access to the transporter. Our mutagenesis analysis suggests that while a large residue is required for maintaining some transporter function, lack of charge also appears to be essential for inhibitor binding. Replacement of W318 with residues present in VMAT2 from other species, except for the phenylalanine mutant, failed to recapitulate any DTBZ binding. Interestingly, of these substitutions, only an arginine was able to fully recapitulate native transport, suggesting lumenal gating activity requires either a large, charged or a large aromatic residue. Our studies also suggest that E127 plays a role in lumenal gating by interacting with LL4 as substitution to alanine-reduced transport, and we speculate that large, charged groups at position 318 directly interact with E127 to maintain full transporter function. In contrast, DBTZ binding remained unaffected for the E127A mutant, suggesting a role for this residue in a later step of transporter closure of the lumenal compartment. Positively charged residues at position 318 may stabilize the lumenal gate and promote conformational cycling through enhanced interactions with negatively charged residues such as E127 but may prevent TBZ from entering the lumenal pathway of the transporter in any capacity. Conservation of this residue in the SLC18 family suggests that this is a common mechanism for lumenal gating. It is unclear what other structural adaptations are present to enable W318 replacement with large positively charged residues in other VMAT2 sequences, but we suspect that the overall architecture of the lumenal domain remains similar. We also note that the disulfide bond between LL1 and -4 plays a critical role in transport (*Yao and Hersh, 2007*), and the disulfide bond may function to restrict the dynamics of this region to allow W318 to occlude the neurotransmitter binding site during transport.

Residues R189 and K138 stand out as critical for drug binding and inhibition and substrate transport. Simulations highlight the role K138 may play in coordinating with the hydroxy group of neurotransmitters and enabling binding at the central site. These results are consistent with previously observed results demonstrating the critical role K138 plays in substrate transport (*Yaffe et al., 2013*; *Merickel et al., 1997*). Remarkably, even mutation to lysine at position 189 abolishes DTBZ binding while still retaining a small amount of transport activity, highlighting the specificity of the DTBZ binding site.

Our structure also provides important clues for understanding the chemical specificity and selectivity of TBZ binding, suggesting that the enhanced affinity of DTBZ is due to preferential interaction with N34. DTBZ is a metabolite of TBZ (*Chen et al., 2012*) which differs by only a hydroxyl group vs. a double bonded oxygen and binds to VMAT2 with approximately twofold higher affinity (*Saida et al., 2023*; *Yao et al., 2011*; *Figure 4a*). Our structure suggests that the amide of N34 acts as a hydrogen bond donor for TBZ, and in the case of DTBZ the hydroxyl of the ligand may act as a hydrogen bond donor for the carbonyl oxygen of N34. We hypothesize that this interaction is more favorable for DTBZ, leading to a higher binding affinity. Valbenazine, a TBZ analogue with a valine attached to the oxygen of the hydroxyl group of DTBZ, binds VMAT2 with a K_d of 150 nM (*Ugolev et al., 2013*; *Uhlyar and Rey, 2018*). We hypothesize that N34 does not form a favorable hydrogen bond with the oxygen of valbenazine and that addition of this larger moiety causes steric clashes in the binding site. Mutation of N34 nearly eliminated DTBZ binding, highlighting its importance in coordinating inhibitor binding. We found N34 is also important for transport, but its precise role remains unclear. Strikingly, replacement with glutamine had no effect on transport whereas aspartate had only a small effect. This suggests that N34 is likely involved in substrate coordination but may not be entirely essential. This is confirmed with the N34A substitution which still showed significant transport activity. In contrast,

a threonine substitution was greatly detrimental, but we believe this is likely due to larger active site perturbations.

Comparison of the residues involved in TBZ binding in VMAT2 vs. VMAT1 also provides insight into the selectivity of TBZ by demonstrating that key differences in the ligand binding site are likely responsible for the reduction in TBZ binding affinity observed in VMAT1 (*Peter et al., 1994*). L37 and V232 are highlighted, and mutation to the equivalent residue in VMAT1, phenylalanine, and leucine, respectively, eliminated DTBZ binding but only reduced substrate transport. Given these results, we suggest these are the primary residues involved in determining TBZ selectivity for VMAT2 vs. VMAT1. We suspect VMAT1 exhibits structural differences compared with VMAT2 to accommodate the larger residues and maintain functional activity.

Through MD simulations, we gained insights into the effects of the protonation states of TBZ and E312. Protonation of TBZ at the amine resulted in an unstable complex, and a structure markedly different from the state resolved with electron microscopy. This suggests TBZ remains unprotonated when bound to the occluded state, as the protonated form will not remain in complex with VMAT2. We believe there may be other TBZ-bound states such as the lumenal-open state where TBZ may be protonated. However, in the terminal complex, E312 must remain protonated suggesting that E312 acts as a hydrogen bond donor to stabilize TBZ in the binding site. Our binding and transport studies further confirm this as the mutation of E312 to glutamine greatly reduces serotonin transport and DTBZ binding (*Figure 4f and g*). Moreover, mutation of E312 to an alanine has long been known to completely negate all TBZ binding and transport activities (*Yaffe et al., 2013*; *Støve et al., 2022*) again highlighting the requirement of hydrogen bond pairing with TBZ.

We also highlight three key polar networks which may be involved in conformational changes induced by proton binding during the transport cycle and are likely also involved in mediating proton transduction (*Figure 6a*). Taken together, we believe these networks play a critical role in mediating the conformation changes taking place in the transporter upon substrate or inhibitor binding. We hypothesize that the protonation of D33, E312, D399, and D426 would significantly perturb these interactions by breaking crucial hydrogen bond pairs and/or salt bridges, leading to opening of the cytosolic gate. This falls in line with previous work highlighting the role these residues play in transport through a variety of mutagenesis and functional experiments (*Merickel et al., 1997*; *Støve et al., 2022*). Given the known transport stoichiometry of two protons per neurotransmitter, we speculate that two protons may dissociate back into the lumen, perhaps driven by the formation of salt bridges between D33 and K138 or R189 and E312 for example in an cytosol-facing state. The asymmetry between these two networks is also striking, with the first network consisting of TM1, -4, and -11 being substantially larger. This may allow for larger conformational changes on this side and an overall asymmetry in the cytosolic-open state of the transporter. To our knowledge, this is also an atypical feature in MFS proteins (*Drew et al., 2021*) and would represent an interesting adaptation upon the rocker-switch mechanism.

Our studies lead us to propose a mechanism by which TBZ inhibits VMAT2 by first entering the transporter from the lumenal-open state and subsequently trapping it in an occluded state through a two-step mechanism centered around W318, which acts as a central plug to close off the lumenal compartment. This provides a basis for non-competitive inhibition as endogenous neurotransmitter is unable to compete for binding from the closed off cytosolic compartment (*Figure 6a*). Our results also provide insight into transporter function, and we propose a mechanism for substrate release from the central binding site (*Figure 6b*). The bound substrate coordinates in the binding site predominantly through interactions with E312 and K138. R189 is directed toward the lumenal space where it engages with one of two water channels. Water enters through these channels into the transporter, passing F135 and F334 and inducing conformational change. In our simulations, we find intrusion of water to cause W318 to flip out of the central site which enables neurotransmitter to dissociate from the transporter (*Figure 6b*).

In summary, we have developed a new fiducial tool incorporating mVenus and the GFP-Nb into the primary sequence of a previously intractable transport protein of great importance to human health. Cryo-EM of VMAT2 allowed us to pinpoint the lumenal and cytoplasmic gates, polar networks likely involved in conformational change and proton transduction, and the conformation and binding site of inhibitors. Our structure facilitated the discovery and detailed analysis of many residues involved in these key molecular mechanisms and enabled further extension in our understanding of

neurotransmitter transport. Thus, by capturing the VMAT2 bound with TBZ along with subsequent mutagenesis, binding, transport, and computational experiments, our work delivers insights into the transporter's mechanism of function and provides a framework for understanding the structural under-pinnings of neurotransmitter release, transport, and inhibition in VMAT2 and other related transport proteins in the MFS family.

Methods

Key resources table

Reagent type (species) or resource	Designation	Source or reference	Identifiers	Additional information
Gene (*Homo sapiens*)	Human vesicular monoamine transporter 2	Clone ID 40025175	NCBI Reference Sequence: BC108928	Horizon Discovery
Gene (*Lama glama*)	Anti-GFP nanobody	Plasmid #49172		Addgene
Cell line (*Homo sapiens*)	HEK293S GnTI⁻	ATCC	Cat # ATCC CRL-3022	Used for expression of VMAT2 (PMID:27929454)
Cell line (*Spodoptera frugiperda*)	Sf9	ATCC	Cat # ATCC CRL-1711	Used in production of baculovirus for transduction (PMID:27929454)
Transfected construct (human)	pEG BacMam	Gouaux lab		PMID:25299155
Affinity chromatography resin	Strep-Tactin Superflow high capacity resin	IBA Lifesciences	Cat # 2-1208-500	Affinity purification resin
Chemical compound, drug	n-Dodecyl-β-D-maltoside	Anatrace	Cat # D310	Detergent
Chemical compound, drug	Cholesteryl hemisuccinate	Anatrace	Cat # CH210	Lipid
Chemical compound, drug	Reserpine	Sigma	Cat # 83580	Inhibitor
Chemical compound, drug	Dihydrotetrabenazine	Cayman Chemicals	Cat # 27182	Inhibitor
Chemical compound, drug	[³H]5-HT	PerkinElmer	Cat # NET1167250UC	Radiolabeled substrate
Chemical compound, drug	[³H]dihydrotetrabenazine	American Radiolabeled Chemicals	Cat # ART 2119	Radiolabeled inhibitor
Chemical compound, drug	Tetrabenazine	Sigma	Cat # T2952	Inhibitor
Chemical compound, detergent	Digitonin	Sigma	Cat # 300410	Detergent
Software, algorithm	Phenix	PMID:22505256	RRID:SCR_014224	https://www.phenix-online.org/
Software, algorithm	SerialEM	PMID:16182563	RRID:SCR_017293	http://bio3d.colorado.edu/SerialEM
Software, algorithm	CryoSPARC	PMID:28165473	RRID:SCR_016501	https://cryosparc.com/
Software, algorithm	RELION	PMID:23000701	RRID:SCR_016274	http://www2.mrc-lmb.cam.ac.uk/relion
Software, algorithm	UCSF-Chimera	PMID:15264254	RRID:SCR_004097	https://www.cgl.ucsf.edu/chimera/
Software, algorithm	Coot	PMID:15572765	RRID:SCR_014222	https://www2.mrc-lmb.cam.ac.uk/personal/pemsley/coot
Software, algorithm	MolProbity	PMID:20057044	RRID:SCR_014226	http://molprobity.biochem.duke.edu/

Continued on next page

Reagent type (species) or resource	Designation	Source or reference	Identifiers	Additional information
Other	R 2/1 200 mesh Au holey carbon grids	Electron Microscopy Sciences	Cat # Q210AR1	Cryo-EM grids
Other	R 1.2/1.3 200 mesh Cu holey carbon grids	Electron Microscopy Sciences	Cat # Q2100CR1.3	Cryo-EM grids
Other	Copper HIS-Tag YSI	PerkinElmer	Cat # RPNQ0096	SPA beads

Data reporting

No statistical methods were used to predetermine sample size. The experiments were not randomized, and the investigators were not blinded to allocation during experiments and outcome assessment.

VMAT2 construct design and cloning

Wild-type VMAT2 was expressed as a C-terminal eGFP fusion protein containing an 8x His-tag. The VMAT2 chimera consisted of mVenus (*Kremers et al., 2006*; *Rothbauer et al., 2008*) fused to the N-terminus of VMAT2 at amino acid position 17, and the anti-GFP nanobody (*Kubala et al., 2010*; *Rothbauer et al., 2008*) containing both a 10x His-tag and a TwinStrep tag fused to the C-terminus at position 482 by Infusion cloning. Single-point mutants were made using PCR starting from wild-type VMAT2 C-terminally tagged eGFP construct, and constructs were initially evaluated using FSEC (*Hattori et al., 2012*).

Expression and purification

VMAT2 was expressed in HEK293S GnTI⁻ cells (*Reeves et al., 2002*) using baculovirus-mediated transduction (*Goehring et al., 2014*). Enriched membranes were first isolated by sonication followed by an initial spin at 10,000×*g* followed by a 100,000×*g* spin and subsequent homogenization. Membranes resuspended in 25 mM Tris pH 8.0 and 150 mM NaCl and frozen at –80°C until use. Membranes were thawed and solubilized in 20 mM *n*-dodecyl-β-D-maltoside (DDM) and 2.5 mM cholesteryl hemisuccinate (CHS) with 1 mM DTT and 10 µM TBZ for 1 hr before centrifugation at 100,000×*g*. VMAT2 was purified into buffer containing 1 mM DDM, 0.125 mM CHS, 25 mM Tris, 150 mM NaCl, 1 mM DTT, and 1 µM TBZ pH 8.0 using either a NiNTA column which was eluted in the same buffer containing 250 mM imidazole (for the wild-type VMAT2 C-terminally tagged eGFP protein) or a StrepTactin column eluted with 5 mM desthiobiotin. Purified VMAT2 was pooled and concentrated using a 100 kDa concentrator (Amicon) before separating by size-exclusion chromatography on a Superose 6 Increase column in 1 mM DDM, 0.125 mM CHS, 25 mM Tris pH 8.0, 150 mM NaCl, 1 mM DTT, and 1 µM TBZ. Peak fractions were pooled, concentrated to 6 mg/ml with a 100 kDa concentrator before addition of 100 µM TBZ, and ultracentrifuged at 60,000×*g* prior to cryo-EM grid preparation.

Cryo-EM sample preparation and data acquisition

The VMAT2 chimera (1.5 µl) at a concentration of 6 mg/ml was applied to glow discharged Quantifoil holey carbon grids (1.2/1.3 or 2/1 200 mesh copper or gold). Grids were blotted for 4 s at 100% humidity, 4°C, with a blot force of 4 using a Vitrobot Mk IV (Thermo Fisher) before flash freezing into a 50/50 mixture of liquid propane/ethane cooled to ~170°C with liquid nitrogen. Videos containing 40 frames were recorded on a FEI Titan Krios operating at 300 kV equipped with a Gatan K3 direct electron detector and a Bioquantum energy filter set to a slit width of 20 eV. Images were collected in super-resolution counting mode at a pixel size of 0.647 Å/pixel with defocus ranges from –1 to –2.5 µm with a total dose of 60 e⁻/Å². Images were recorded using SerialEM (*Mastronarde, 2003*).

Image processing

Micrographs were corrected using Patch Motion Correction and contrast transfer function estimated using Patch CTF in CryoSPARC v4.2 (*Punjani et al., 2017*). A total of 24,875 micrographs were collected between two datasets recorded on the same microscope. Particles were initially classified by 2D classification in CryoSPARC to generate an ab initio model for template picking which resulted in ~10 million picks which were extracted at a box size of 384 binned to 128 and classified

multiple times using 2D classification and hetero-refinement using a newly generated ab initio model, an empty detergent 'decoy' class, and a junk class containing random density. The resulting approximately 500,000 particles from each dataset were re-extracted at a box size of 384 binned to 256, refined using non-uniform refinement (*Punjani et al., 2020*), and combined before being subjected to further classification and refinement. The remaining 212k particles were then re-extracted at a full box size of 384, refined, and subjected to Bayesian polishing in RELION 3.1 (*Scherman et al., 1983*; *Scheres, 2012*). The resulting 3.5 Å map still exhibited significant anisotropy and was subjected to further rounds of 3D classification and refinement in CryoSPARC with a TMD mask to improve features of the peripheral TMs. The final 65,516 particles resulted in a 3.12 Å map that was sharpened in Deep-EMhancer (*Sanchez-Garcia et al., 2021*) using the mask setting and utilizing a mask around the TMD only.

Model building

The resulting EM map was sufficient for modeling most VMAT2 side chains in the TMD. The Alpha-Fold2 (*Jumper et al., 2021*) model of VMAT2 was used for initial fitting and was further refined using RosettaCM (*Wang et al., 2016*). After successive rounds of RosettaCM, the model was locally fit using Coot 0.98 (*Emsley and Cowtan, 2004*) and Isolde (*Croll, 2018*) with the majority of the manual rebuilding being done in Isolde. The model was refined in real space using Phenix 1.2 (*Liebschner et al., 2019*) and validated by comparing the FSC between the half maps and the refined model.

Radioligand binding assays

Purified VMAT2 (wild-type eGFP tagged and VMAT2 chimera) were diluted to 5 nM in 1 mM DDM, 0.125 mM CHS in 20 mM Tris pH 8.0, 150 mM NaCl with 1 mg/ml CuYSi beads (PerkinElmer). Protein concentration was estimated using FSEC and a standard GFP concentration curve. Protein was then mixed 1:1 to a final protein concentration of 2.5 nM in detergent buffer containing serially diluted ^{3}H-labeled DTBZ (American Radiolabeled Chemicals) starting at 60 nM final concentration. Counts were then measured using a Microbeta2 scintillation counter in 96-well plates with triplicate measurements (*Green et al., 2015*). Specific counts were obtained by subtracting values obtained by the addition of 100 µM reserpine. Mutants were evaluated similarly from cell lysates of transfected cells. Data were fit to a single-site binding equation using GraphPad Prism.

Competition binding experiments were performed at the same protein concentration in the same detergent buffer. 10 nM ^{3}H-labeled DTBZ was added to buffer and used for nine 1:1 serial dilutions with detergent buffer which initially contained 100 µM reserpine (10 µM for chimera). Measurements were done in triplicates and fit with a one-site competitive binding equation in GraphPad Prism.

Serotonin transport

Cells transduced overnight were spun down and resuspended in 140 mM KCl, 5 mM MgCl$_2$, 50 mM HEPES-KOH pH 7.4, and 0.3 M sucrose. Cells were permeabilized at 30°C for 10 min in the presence of 5 mM MgATP and 0.01% digitonin (*Yaffe et al., 2016*). Controls additionally included 100 µM reserpine. After 10 min, cells were spun down and resuspended in the same buffer containing 2.5 mM MgATP and incubated at 30°C for 10 min. Cells were then mixed 1:1 with buffer containing ^{3}H-labeled serotonin at a final concentration of 1 or 10 µM and incubated at room temperature for 6 min. Transport was stopped by the addition of ice-cold buffer, and the cells were collected on Glass Fiber C filters. The filters were then counted in scintillation fluid. Time course experiments were performed in the same way using 1 µM serotonin.

To evaluate mutants, ~5 million cells were transfected with 5 µg of DNA using Polyjet reagent. 24 hr after transfection, the cells were harvested into assay buffer containing 130 mM KCl, 5 mM MgCl$_2$, 25 mM HEPES-KOH pH 7.4, 1 mM ascorbic acid, 5 mM glucose, and washed once with 1 ml of assay buffer. Cells were permeabilized in 500 µl of assay buffer containing 0.001% digitonin and washed once with 1 ml of assay buffer. Next the cells were resuspended, mixed 1:1 with of 0.2 µM ^{3}H-labeled serotonin with 5 mM ATP in assay buffer, and incubated at room temperature for 15 min. In some cases, 12.5 µM reserpine was added to the cells along with ^{3}H-labeled serotonin for a control. Cells were washed with 2 ml of ice-cold assay buffer and solubilized with 5% Triton X-100 followed by scintillation counting. Mutant expression was assessed with fluorescent microscopy to ensure protein expression levels were comparable.

MD simulations

The initial MD simulation system was prepared using CHARMM-GUI Membrane Builder module (*Wu et al., 2014*). The structure of VMAT2 bound to TBZ was aligned using PPM2.0 webserver (*Lomize et al., 2012*) and embedded into 1-palmitoyl-2-oleoyl-*sn*-glycero-3-phosphocholine (POPC) membrane lipids. The pK_a values of titratable residues of VMAT2 in the presence or absence of TBZ were calculated using PROPKA 3.5.0 (*Olsson et al., 2011*); and the computed pK_a values for acidic residues and TBZ are listed in *Table 4*. Of note, D33 and E312, as well as D399 and D426 (yellow highlights in *Figure 5—figure supplement 1c* and bold in *Table 4*) are in proximity to TBZ; thus, their protonation states may impact substantially TBZ binding. Given that D33 may form a salt bridge with its nearby K138, we assumed it to be deprotonated; and E312 and D399 were assumed to be protonated because of their comparatively higher pK_a values. To further assess how the protonation states on TBZ and/or D426 affect the binding propensity of TBZ, we constructed four different simulation systems (see *Table 3*) with either protonated or deprotonated TBZ and with/without protonation of D426 (in addition to E312 and D399), denoted as systems TBZ_1–TBZ_4. For each system, TIP3P waters and K$^+$ and Cl$^-$ ions corresponding to 0.1 M KCl solution were added to build a simulation box of 92×92×108 Å^3. The simulated systems contained approximately 86,000 atoms, including VMAT2 and TBZ, 203 POPC molecules, and 17,400 water molecules.

All MD simulations were performed using NAMD (*Phillips et al., 2005*) (version NAMD_2.13), following default protocol and parameters implemented in CHARMM-GUI (*Lee et al., 2016*). Briefly, CHARMM36 force fields were adopted for VMAT2, lipids, and water molecules (*Klauda et al., 2010*; *Huang et al., 2017*). Force field parameters for both protonated (carried +1 charge) and neutral-charged TBZ were obtained from the CHARMM General Force Field for drug-like molecules (*Vanommeslaeghe et al., 2012*); and proton was added using Open Babel (*O'Boyle et al., 2011*). Prior to productive runs, the simulation systems were energy-minimized for 10,000 steps, followed by 2 ns (*Hoover, 1985*; *Nosé, 1984*) constant pressure (1 bar, 310 K; NPT) simulation during which the constraints on the protein backbone were reduced from 10 to 0 kcal/mol. Finally, the unconstrained protein was subjected to 100–180 ns NPT simulations. Periodic boundary conditions were employed in all simulations, and the particle mesh Ewald method (*Essmann et al., 1995*) was used for long-range electrostatic interactions with the pair list distance of 16.0 Å. The simulation time step was set to 2 fs with the covalent hydrogen bonds constrained with the SHAKE algorithm (*Ryckaert et al., 1977*). A force-based switching function was used for Lennard-Jones interactions with switching distance set to 10 Å. Langevin dynamics was applied with a piston period of 50 fs and a piston decay of 25 fs, as well as Langevin temperature coupling with a friction coefficient of 1 ps^{-1}. For each system, two to three independent runs of 100–180 ns were performed (see *Table 3*). Snapshots from trajectories were recorded every 100 ps for statistical analysis interactions and structural changes.

For DA bound to the occluded VMAT2, we constructed five simulation systems with varying protonation states for the four pocket-lining acidic residues (denoted as runs DA_0 to DA_4; see *Table 5*). In all systems, the DA carried +1 charge and was initially positioned at the top (lowest energy) docking-predicted binding pose (see *Figure 5—figure supplement 1*); and for each system, two runs of 100 ns were performed, following the same simulation protocols described above for TBZ, except for an extended run of 200 ns conducted to visualize the DA release to the SV lumen, which comprised 170 ns conventional MD simulations, followed by 4 ns of enhanced conformation sampling using the adaptive biasing force method (*Cheng et al., 2018*; *Chipot and Hénin, 2005*), and subsequent 30 ns conventional MD simulations.

Docking simulations

The binding of DA, serotonin, and TBZ to the AlphaFold2-modeled VMAT2 conformer (AF-Q05940-F1-model_v4) and to the present cryo-EM-resolved structure were simulated using AutoDock Vina (*Trott and Olson, 2010*). The molecular structures of protonated DA and serotonin were adopted from the previous studies (*Cheng et al., 2015*; *Yang and Gouaux, 2021*). Docking simulations were carried out using a grid with dimensions set to 65×65×70 Å^3 to encapsulate the entire structure of the transporter. The exhaustiveness of the simulation was set to 50, and the algorithm returned a maximum of 20 ligand binding poses.

Computational data analysis

MD trajectory analysis and visualization were performed using VMD (*Humphrey et al., 1996*). For each snapshot, the TBZ binding affinity was evaluated using contact-based binding affinity predictor PRODIGY-LIG (*Vangone et al., 2019*); and the number of waters within the TBZ binding pocket were assessed by counting the number of oxygen (OH_2) atoms within 3.5 Å of TBZ. For RMSD calculations, the C^α-atoms of VMAT2 and the heavy atoms from TBZ were used after alignment of the simulated VAMT2 onto the cryo-EM structure. The binding pockets of VMAT2 were assessed using Essential Site Scanning Analysis (ESSA) (*Kaynak et al., 2020*) and Fpocket (*Le Guilloux et al., 2009*), implemented in ProDy 2.0 (*Zhang et al., 2021*). Sequence conservation of VMAT2 was computed using the ConSurf server with default parameters (*Yariv et al., 2023*). Multiple sequence alignment for SLC18 family members was performed using PROMALS3D (*Pei et al., 2008*).

Acknowledgements

Additional information

Funding

Author contributions

Michael P Dalton, Conceptualization, Data curation, Validation, Investigation, Visualization, Methodology, Writing – original draft, Writing – review and editing; Mary Hongying Cheng, Data curation, Validation, Investigation, Visualization, Methodology, Writing – original draft, Writing – review and editing; Ivet Bahar, Supervision, Funding acquisition, Methodology, Project administration, Writing – review and editing; Jonathan A Coleman, Conceptualization, Resources, Data curation, Supervision, Funding acquisition, Validation, Investigation, Visualization, Methodology, Writing – original draft, Project administration, Writing – review and editing

Author ORCIDs

Michael P Dalton ⓘ http://orcid.org/0000-0001-5296-5099
Mary Hongying Cheng ⓘ http://orcid.org/0000-0001-5833-8221
Jonathan A Coleman ⓘ https://orcid.org/0000-0003-0001-6195

Peer review material

Reviewer #1 (Public Review): https://doi.org/10.7554/eLife.91973.4.sa1
Reviewer #2 (Public Review): https://doi.org/10.7554/eLife.91973.4.sa2
Reviewer #3 (Public Review): https://doi.org/10.7554/eLife.91973.4.sa3
Author Response https://doi.org/10.7554/eLife.91973.4.sa4

Data availability

The coordinates and associated volumes for the cryo-EM reconstruction of the VMAT2-TBZ data set have been deposited in the Protein Data Bank (PDB) and Electron Microscopy Data Bank (EMDB) under the accession codes 8THR and 41269.

The following datasets were generated:

Author(s)	Year	Dataset title	Dataset URL	Database and Identifier
Dalton MP, Coleman JA	2023	Structure of the human vesicular monoamine transporter 2 (VMAT2) bound to tetrabenazine in an occluded conformation	https://www.rcsb.org/structure/8THR	RCSB Protein Data Bank, 8THR
Dalton MP, Coleman JA	2023	Structure of the human vesicular monoamine transporter 2 (VMAT2) bound to Tetrabenazine in an occluded conformation	https://www.ebi.ac.uk/emdb/EMD-41269	Electron Microscopy Data Bank, EMD-41269

References

Arvidsson U, Riedl M, Elde R, Meister B. 1997. Vesicular acetylcholine transporter (VAChT) protein: a novel and unique marker for cholinergic neurons in the central and peripheral nervous systems. *The Journal of Comparative Neurology* **378**:454–467 PMID: 9034903.

Bohnen NI, Albin RL, Koeppe RA, Wernette KA, Kilbourn MR, Minoshima S, Frey KA. 2006. Positron emission tomography of monoaminergic vesicular binding in aging and Parkinson disease. *Journal of Cerebral Blood Flow and Metabolism* **26**:1198–1212. DOI: https://doi.org/10.1038/sj.jcbfm.9600276, PMID: 16421508

Carlsson A, Lindqvist M, Manusson T. 1957. 3,4-Dihydroxyphenylalanine and 5-hydroxytryptophan as reserpine antagonists. *Nature* **180**:1200. DOI: https://doi.org/10.1038/1801200a0, PMID: 13483658

Chen JJ, Ondo WG, Dashtipour K, Swope DM. 2012. Tetrabenazine for the treatment of hyperkinetic movement disorders: a review of the literature. *Clinical Therapeutics* **34**:1487–1504. DOI: https://doi.org/10.1016/j.clinthera.2012.06.010, PMID: 22749259

Chen H, Ahmed S, Zhao H, Elghobashi-Meinhardt N, Dai Y, Kim JH, McDonald JG, Li X, Lee CH. 2023. Structural and functional insights into Spns2-mediated transport of sphingosine-1-phosphate. *Cell* **186**:2644–2655. DOI: https://doi.org/10.1016/j.cell.2023.04.028, PMID: 37224812

Cheng MH, Block E, Hu F, Cobanoglu MC, Sorkin A, Bahar I. 2015. Insights into the modulation of dopamine transporter function by amphetamine, orphenadrine, and cocaine binding. *Frontiers in Neurology* **6**:134. DOI: https://doi.org/10.3389/fneur.2015.00134, PMID: 26106364

Cheng MH, Kaya C, Bahar I. 2018. Quantitative assessment of the energetics of dopamine translocation by human dopamine transporter. *The Journal of Physical Chemistry. B* **122**:5336–5346. DOI: https://doi.org/10.1021/acs.jpcb.7b10340, PMID: 29232131

Chipot C, Hénin J. 2005. Exploring the free-energy landscape of a short peptide using an average force. *The Journal of Chemical Physics* **123**:244906. DOI: https://doi.org/10.1063/1.2138694, PMID: 16396572

Croll TI. 2018. *ISOLDE*: a physically realistic environment for model building into low-resolution electron-density maps. *Acta Crystallographica Section D Structural Biology* **74**:519–530. DOI: https://doi.org/10.1107/S2059798318002425

Drew D, North RA, Nagarathinam K, Tanabe M. 2021. Structures and general transport mechanisms by the major facilitator superfamily (MFS). *Chemical Reviews* **121**:5289–5335. DOI: https://doi.org/10.1021/acs.chemrev.0c00983, PMID: 33886296

Eiden LE. 2000. The vesicular neurotransmitter transporters: current perspectives and future prospects. *FASEB Journal* **14**:2396–2400. DOI: https://doi.org/10.1096/fj.00-0817rev, PMID: 11099457

Eiden LE, Schäfer MKH, Weihe E, Schütz B. 2004. The vesicular amine transporter family (SLC18): amine/proton antiporters required for vesicular accumulation and regulated exocytotic secretion of monoamines and acetylcholine. *Pflugers Archiv* **447**:636–640. DOI: https://doi.org/10.1007/s00424-003-1100-5, PMID: 12827358

Eiden LE, Weihe E. 2011. VMAT2: a dynamic regulator of brain monoaminergic neuronal function interacting with drugs of abuse. *Annals of the New York Academy of Sciences* **1216**:86–98. DOI: https://doi.org/10.1111/j.1749-6632.2010.05906.x, PMID: 21272013

Emsley P, Cowtan K. 2004. Coot: model-building tools for molecular graphics. *Acta Crystallographica. Section D, Biological Crystallography* **60**:2126–2132. DOI: https://doi.org/10.1107/S0907444904019158, PMID: 15572765

Erickson JD, Eiden LE, Hoffman BJ. 1992. Expression cloning of a reserpine-sensitive vesicular monoamine transporter. *PNAS* **89**:10993–10997. DOI: https://doi.org/10.1073/pnas.89.22.10993

Erickson JD, Schafer MK, Bonner TI, Eiden LE, Weihe E. 1996. Distinct pharmacological properties and distribution in neurons and endocrine cells of two isoforms of the human vesicular monoamine transporter. *PNAS* **93**:5166–5171. DOI: https://doi.org/10.1073/pnas.93.10.5166

Essmann U, Perera L, Berkowitz ML, Darden T, Lee H, Pedersen LG. 1995. A smooth particle mesh Ewald method. *The Journal of Chemical Physics* **103**:8577–8593. DOI: https://doi.org/10.1063/1.470117

Fehr C, Sommerlad D, Sander T, Anghelescu I, Dahmen N, Szegedi A, Mueller C, Zill P, Soyka M, Preuss UW. 2013. Association of VMAT2 gene polymorphisms with alcohol dependence. *Journal of Neural Transmission* **120**:1161–1169. DOI: https://doi.org/10.1007/s00702-013-0996-y, PMID: 23504072

Fon EA, Pothos EN, Sun BC, Killeen N, Sulzer D, Edwards RH. 1997. Vesicular transport regulates monoamine storage and release but is not essential for amphetamine action. *Neuron* **19**:1271–1283. DOI: https://doi.org/10.1016/s0896-6273(00)80418-3, PMID: 9427250

Freyberg Z, Sonders MS, Aguilar JI, Hiranita T, Karam CS, Flores J, Pizzo AB, Zhang Y, Farino ZJ, Chen A, Martin CA, Kopajtic TA, Fei H, Hu G, Lin YY, Mosharov EV, McCabe BD, Freyberg R, Wimalasena K, Hsin LW, et al. 2016. Mechanisms of amphetamine action illuminated through optical monitoring of dopamine synaptic vesicles in *Drosophila* brain. *Nature Communications* **7**:10652. DOI: https://doi.org/10.1038/ncomms10652, PMID: 26879809

Goehring A, Lee C-H, Wang KH, Michel JC, Claxton DP, Baconguis I, Althoff T, Fischer S, Garcia KC, Gouaux E. 2014. Screening and large-scale expression of membrane proteins in mammalian cells for structural studies. *Nature Protocols* **9**:2574–2585. DOI: https://doi.org/10.1038/nprot.2014.173, PMID: 25299155

Green EM, Coleman JA, Gouaux E. 2015. Thermostabilization of the human serotonin transporter in an antidepressant-bound conformation. *PLOS ONE* **10**:e0145688. DOI: https://doi.org/10.1371/journal.pone.0145688, PMID: 26695939

Han H, Xia X, Zheng H, Zhao C, Xu Y, Tao J, Wang X. 2020. The Gene Polymorphism of VMAT2 Is Associated with risk of schizophrenia in male han chinese. *Psychiatry Investigation* **17**:1073–1078. DOI: https://doi.org/10.30773/pi.2020.0023, PMID: 33099987

Hattori M, Hibbs RE, Gouaux E. 2012. A fluorescence-detection size-exclusion chromatography-based thermostability assay for membrane protein precrystallization screening. *Structure* **20**:1293–1299. DOI: https://doi.org/10.1016/j.str.2012.06.009, PMID: 22884106

Henry JP, Sagné C, Bedet C, Gasnier B. 1998. The vesicular monoamine transporter: from chromaffin granule to brain. *Neurochemistry International* **32**:227–246. DOI: https://doi.org/10.1016/s0197-0186(97)00092-2, PMID: 9587917

Hiasa M, Miyaji T, Haruna Y, Takeuchi T, Harada Y, Moriyama S, Yamamoto A, Omote H, Moriyama Y. 2014. Identification of a mammalian vesicular polyamine transporter. *Scientific Reports* **4**:6836. DOI: https://doi.org/10.1038/srep06836, PMID: 25355561

Hoover WG. 1985. Canonical dynamics: Equilibrium phase-space distributions. *Physical Review. A, General Physics* **31**:1695–1697. DOI: https://doi.org/10.1103/physreva.31.1695, PMID: 9895674

Huang J, Rauscher S, Nawrocki G, Ran T, Feig M, de Groot BL, Grubmüller H, MacKerell AD Jr. 2017. CHARMM36m: an improved force field for folded and intrinsically disordered proteins. *Nature Methods* **14**:71–73. DOI: https://doi.org/10.1038/nmeth.4067, PMID: 27819658

Humphrey W, Dalke A, Schulten K. 1996. VMD: visual molecular dynamics. *Journal of Molecular Graphics* **14**:33–38, . DOI: https://doi.org/10.1016/0263-7855(96)00018-5, PMID: 8744570

Jacobsen JC, Wilson C, Cunningham V, Glamuzina E, Prosser DO, Love DR, Burgess T, Taylor J, Swan B, Hill R, Robertson SP, Snell RG, Lehnert K. 2016. Brain dopamine-serotonin vesicular transport disease presenting as a severe infantile hypotonic parkinsonian disorder. *Journal of Inherited Metabolic Disease* **39**:305–308. DOI: https://doi.org/10.1007/s10545-015-9897-6, PMID: 26497564

Jardetzky O. 1966. Simple allosteric model for membrane pumps. *Nature* **211**:969–970. DOI: https://doi.org/10.1038/211969a0, PMID: 5968307

Johnson RG. 1988. Accumulation of biological amines into chromaffin granules: a model for hormone and neurotransmitter transport. *Physiological Reviews* **68**:232–307. DOI: https://doi.org/10.1152/physrev.1988.68.1.232, PMID: 2892215

Jumper J, Evans R, Pritzel A, Green T, Figurnov M, Ronneberger O, Tunyasuvunakool K, Bates R, Žídek A, Potapenko A, Bridgland A, Meyer C, Kohl SAA, Ballard AJ, Cowie A, Romera-Paredes B, Nikolov S, Jain R, Adler J, Back T, et al. 2021. Highly accurate protein structure prediction with AlphaFold. *Nature* **596**:583–589. DOI: https://doi.org/10.1038/s41586-021-03819-2, PMID: 34265844

Kaur N, Kumar P, Jamwal S, Deshmukh R, Gauttam VT. 2016. Tetrabenazine: Spotlight on drug review. *Annals of Neurosciences* **23**:176–185. DOI: https://doi.org/10.1159/000449184

Kaynak BT, Bahar I, Doruker P. 2020. Essential site scanning analysis: A new approach for detecting sites that modulate the dispersion of protein global motions. *Computational and Structural Biotechnology Journal* **18**:1577–1586. DOI: https://doi.org/10.1016/j.csbj.2020.06.020, PMID: 32637054

Kirshner N. 1962. Uptake of catecholamines by a particulate fraction of the adrenal medulla. *The Journal of Biological Chemistry* **237**:2311–2317 PMID: 14456353.

Klauda JB, Venable RM, Freites JA, O'Connor JW, Tobias DJ, Mondragon-Ramirez C, Vorobyov I, MacKerell AD Jr, Pastor RW. 2010. Update of the CHARMM all-atom additive force field for lipids: validation on six lipid types. *The Journal of Physical Chemistry. B* **114**:7830–7843. DOI: https://doi.org/10.1021/jp101759q, PMID: 20496934

Kremers GJ, Goedhart J, van Munster EB, Gadella TJ. 2006. Cyan and yellow super fluorescent proteins with improved brightness, protein folding, and FRET Förster radius. *Biochemistry* **45**:6570–6580. DOI: https://doi.org/10.1021/bi0516273, PMID: 16716067

Kubala MH, Kovtun O, Alexandrov K, Collins BM. 2010. Structural and thermodynamic analysis of the GFP:GFP-nanobody complex. *Protein Science* **19**:2389–2401. DOI: https://doi.org/10.1002/pro.519, PMID: 20945358

Lee J, Cheng X, Swails JM, Yeom MS, Eastman PK, Lemkul JA, Wei S, Buckner J, Jeong JC, Qi Y, Jo S, Pande VS, Case DA, Brooks CL, MacKerell AD, Klauda JB, Im W. 2016. CHARMM-GUI input generator for NAMD, GROMACS, AMBER, OpenMM, and CHARMM/OpenMM simulations using the CHARMM36 additive force field. *Journal of Chemical Theory and Computation* **12**:405–413. DOI: https://doi.org/10.1021/acs.jctc.5b00935, PMID: 26631602

Le Guilloux V, Schmidtke P, Tuffery P. 2009. Fpocket: an open source platform for ligand pocket detection. *BMC Bioinformatics* **10**:168. DOI: https://doi.org/10.1186/1471-2105-10-168, PMID: 19486540

Li F, Eriksen J, Finer-Moore J, Chang R, Nguyen P, Bowen A, Myasnikov A, Yu Z, Bulkley D, Cheng Y, Edwards RH, Stroud RM. 2020. Ion transport and regulation in a synaptic vesicle glutamate transporter. *Science* **368**:893–897. DOI: https://doi.org/10.1126/science.aba9202, PMID: 32439795

Liebschner D, Afonine PV, Baker ML, Bunkóczi G, Chen VB, Croll TI, Hintze B, Hung L-W, Jain S, McCoy AJ, Moriarty NW, Oeffner RD, Poon BK, Prisant MG, Read RJ, Richardson JS, Richardson DC, Sammito MD, Sobolev OV, Stockwell DH, et al. 2019. Macromolecular structure determination using X-rays, neutrons and electrons: recent developments in *Phenix* . *Acta Crystallographica Section D Structural Biology* **75**:861–877. DOI: https://doi.org/10.1107/S2059798319011471

Liu Y, Peter D, Roghani A, Schuldiner S, Privé GG, Eisenberg D, Brecha N, Edwards RH. 1992. A cDNA that suppresses MPP+ toxicity encodes A vesicular amine transporter. *Cell* **70**:539–551. DOI: https://doi.org/10.1016/0092-8674(92)90425-c, PMID: 1505023

Lohoff FW, Dahl JP, Ferraro TN, Arnold SE, Gallinat J, Sander T, Berrettini WH. 2006. Variations in the vesicular monoamine transporter 1 gene (VMAT1/SLC18A1) are associated with bipolar i disorder. *Neuropsychopharmacology* **31**:2739–2747. DOI: https://doi.org/10.1038/sj.npp.1301196, PMID: 16936705

Lohoff FW, Weller AE, Bloch PJ, Buono RJ, Doyle GA, Ferraro TN, Berrettini WH. 2008. Association between polymorphisms in the vesicular monoamine transporter 1 gene (VMAT1/SLC18A1) on chromosome 8p and schizophrenia. *Neuropsychobiology* **57**:55–60. DOI: https://doi.org/10.1159/000129668, PMID: 18451639

Lomize MA, Pogozheva ID, Joo H, Mosberg HI, Lomize AL. 2012. OPM database and PPM web server: resources for positioning of proteins in membranes. *Nucleic Acids Research* **40**:D370–D376. DOI: https://doi.org/10.1093/nar/gkr703, PMID: 21890895

Mastronarde DN. 2003. SerialEM: a program for automated tilt series acquisition on tecnai microscopes using prediction of specimen position. *Microscopy and Microanalysis* **9**:1182–1183. DOI: https://doi.org/10.1017/S1431927603445911

Merickel A, Kaback HR, Edwards RH. 1997. Charged residues in transmembrane domains II and XI of a vesicular monoamine transporter form a charge pair that promotes high affinity substrate recognition. *The Journal of Biological Chemistry* **272**:5403–5408. DOI: https://doi.org/10.1074/jbc.272.9.5403, PMID: 9038139

Mitchell P. 1957. A general theory of membrane transport from studies of bacteria. *Nature* **180**:134–136. DOI: https://doi.org/10.1038/180134a0, PMID: 13451664

Mukherjee S, Erramilli SK, Ammirati M, Alvarez FJD, Fennell KF, Purdy MD, Skrobek BM, Radziwon K, Coukos J, Kang Y, Dutka P, Gao X, Qiu X, Yeager M, Eric Xu H, Han S, Kossiakoff AA. 2020. Synthetic antibodies against BRIL as universal fiducial marks for single−particle cryoEM structure determination of membrane proteins. *Nature Communications* **11**:1598. DOI: https://doi.org/10.1038/s41467-020-15363-0

Nosé S. 1984. A molecular dynamics method for simulations in the canonical ensemble. *Molecular Physics* **52**:255–268. DOI: https://doi.org/10.1080/00268978400101201

O'Boyle NM, Banck M, James CA, Morley C, Vandermeersch T, Hutchison GR. 2011. Open Babel: An open chemical toolbox. *Journal of Cheminformatics* **3**:33. DOI: https://doi.org/10.1186/1758-2946-3-33

Olsson MHM, Søndergaard CR, Rostkowski M, Jensen JH. 2011. PROPKA3: consistent treatment of internal and surface residues in empirical pKa predictions. *Journal of Chemical Theory and Computation* **7**:525–537. DOI: https://doi.org/10.1021/ct100578z, PMID: 26596171

Padmakumar M, Jaeken J, Ramaekers V, Lagae L, Greene D, Thys C, Van Geet C, BioResource N, Stirrups K, Downes K, Turro E, Freson K. 2019. A novel missense variant in *SLC18A2* causes recessive brain monoamine vesicular transport disease and absent serotonin in platelets. *JIMD Reports* **47**:9–16. DOI: https://doi.org/10.1002/jmd2.12030, PMID: 31240161

Pei J, Kim BH, Grishin NV. 2008. PROMALS3D: a tool for multiple protein sequence and structure alignments. *Nucleic Acids Research* **36**:2295–2300. DOI: https://doi.org/10.1093/nar/gkn072, PMID: 18287115

Peter D, Jimenez J, Liu Y, Kim J, Edwards RH. 1994. The chromaffin granule and synaptic vesicle amine transporters differ in substrate recognition and sensitivity to inhibitors. *The Journal of Biological Chemistry* **269**:7231–7237 PMID: 8125935.

Peter D, Liu Y, Sternini C, de Giorgio R, Brecha N, Edwards RH. 1995. Differential expression of two vesicular monoamine transporters. *The Journal of Neuroscience* **15**:6179–6188. DOI: https://doi.org/10.1523/JNEUROSCI.15-09-06179.1995, PMID: 7666200

Phillips JC, Braun R, Wang W, Gumbart J, Tajkhorshid E, Villa E, Chipot C, Skeel RD, Kalé L, Schulten K. 2005. Scalable molecular dynamics with NAMD. *Journal of Computational Chemistry* **26**:1781–1802. DOI: https://doi.org/10.1002/jcc.20289, PMID: 16222654

Punjani A, Rubinstein JL, Fleet DJ, Brubaker MA. 2017. cryoSPARC: algorithms for rapid unsupervised cryo-EM structure determination. *Nature Methods* **14**:290–296. DOI: https://doi.org/10.1038/nmeth.4169, PMID: 28165473

Punjani A, Zhang H, Fleet DJ. 2020. Non-uniform refinement: adaptive regularization improves single-particle cryo-EM reconstruction. *Nature Methods* **17**:1214–1221. DOI: https://doi.org/10.1038/s41592-020-00990-8, PMID: 33257830

Radestock S, Forrest LR. 2011. The alternating-access mechanism of MFS transporters arises from inverted-topology repeats. *Journal of Molecular Biology* **407**:698–715. DOI: https://doi.org/10.1016/j.jmb.2011.02.008, PMID: 21315728

Reeves PJ, Callewaert N, Contreras R, Khorana HG. 2002. Structure and function in rhodopsin: high-level expression of rhodopsin with restricted and homogeneous N-glycosylation by a tetracycline-inducible N-acetylglucosaminyltransferase I-negative HEK293S stable mammalian cell line. *PNAS* **99**:13419–13424. DOI: https://doi.org/10.1073/pnas.212519299, PMID: 12370423

Rilstone JJ, Alkhater RA, Minassian BA. 2013. Brain dopamine-serotonin vesicular transport disease and its treatment. *The New England Journal of Medicine* **368**:543–550. DOI: https://doi.org/10.1056/NEJMoa1207281, PMID: 23363473

Rothbauer U, Zolghadr K, Muyldermans S, Schepers A, Cardoso MC, Leonhardt H. 2008. A versatile nanotrap for biochemical and functional studies with fluorescent fusion proteins. *Molecular & Cellular Proteomics* **7**:282–289. DOI: https://doi.org/10.1074/mcp.M700342-MCP200, PMID: 17951627

Ryckaert JP, Ciccotti G, Berendsen HJC. 1977. Numerical integration of the cartesian equations of motion of a system with constraints: molecular dynamics of n-alkanes. *Journal of Computational Physics* **23**:327–341. DOI: https://doi.org/10.1016/0021-9991(77)90098-5

Saida K, Maroofian R, Sengoku T, Mitani T, Pagnamenta AT, Marafi D, Zaki MS, O'Brien TJ, Karimiani EG, Kaiyrzhanov R, Takizawa M, Ohori S, Leong HY, Akay G, Galehdari H, Zamani M, Romy R, Carroll CJ, Toosi MB, Ashrafzadeh F, et al. 2023. Brain monoamine vesicular transport disease caused by homozygous SLC18A2 variants: A study in 42 affected individuals. *Genetics in Medicine* **25**:90–102. DOI: https://doi.org/10.1016/j.gim.2022.09.010, PMID: 36318270

Sanchez-Garcia R, Gomez-Blanco J, Cuervo A, Carazo JM, Sorzano COS, Vargas J. 2021. DeepEMhancer: a deep learning solution for cryo-EM volume post-processing. *Communications Biology* **4**:874. DOI: https://doi.org/10.1038/s42003-021-02399-1, PMID: 34267316

Scheres SHW. 2012. RELION: implementation of a Bayesian approach to cryo-EM structure determination. *Journal of Structural Biology* **180**:519–530. DOI: https://doi.org/10.1016/j.jsb.2012.09.006, PMID: 23000701

Scherman D, Jaudon P, Henry JP. 1983. Characterization of the monoamine carrier of chromaffin granule membrane by binding of [2-3H]dihydrotetrabenazine. *PNAS* **80**:584–588. DOI: https://doi.org/10.1073/pnas.80.2.584

Scherman D, Henry JP. 1984. Reserpine binding to bovine chromaffin granule membranes: characterization and comparison with dihydrotetrabenazine binding. *Molecular Pharmacology* **25**:113–122 PMID: 6708929.

Schrödinger. 2023. *Schrödinger Release 2023-4: Maestro*. Schrödinger LLC.

Schuldiner S, Shirvan A, Linial M. 1995. Vesicular neurotransmitter transporters: from bacteria to humans. *Physiological Reviews* **75**:369–392. DOI: https://doi.org/10.1152/physrev.1995.75.2.369, PMID: 7724667

Simons CJP, van Winkel R, GROUP. 2013. Intermediate phenotype analysis of patients, unaffected siblings, and healthy controls identifies VMAT2 as a candidate gene for psychotic disorder and neurocognition. *Schizophrenia Bulletin* **39**:848–856. DOI: https://doi.org/10.1093/schbul/sbs067

Støve SI, Skjevik ÅA, Teigen K, Martinez A. 2022. Inhibition of VMAT2 by β2-adrenergic agonists, antagonists, and the atypical antipsychotic ziprasidone. *Communications Biology* **5**:1283. DOI: https://doi.org/10.1038/s42003-022-04121-1, PMID: 36418492

Takahashi N, Miner LL, Sora I, Ujike H, Revay RS, Kostic V, Jackson-Lewis V, Przedborski S, Uhl GR. 1997. VMAT2 knockout mice: Heterozygotes display reduced amphetamine-conditioned reward, enhanced amphetamine locomotion, and enhanced MPTP toxicity. *PNAS* **94**:9938–9943. DOI: https://doi.org/10.1073/pnas.94.18.9938

Thiriot DS, Ruoho AE. 2001. Mutagenesis and derivatization of human vesicle monoamine transporter 2 (VMAT2) cysteines identifies transporter domains involved in tetrabenazine binding and substrate transport. *The Journal of Biological Chemistry* **276**:27304–27315. DOI: https://doi.org/10.1074/jbc.M103947200, PMID: 11375404

Thiriot DS, Sievert MK, Ruoho AE. 2002. Identification of human vesicle monoamine transporter (VMAT2) lumenal cysteines that form an intramolecular disulfide bond. *Biochemistry* **41**:6346–6353. DOI: https://doi.org/10.1021/bi015779j, PMID: 12009896

Trott O, Olson AJ. 2010. AutoDock Vina: Improving the speed and accuracy of docking with a new scoring function, efficient optimization, and multithreading. *Journal of Computational Chemistry* **31**:455–461. DOI: https://doi.org/10.1002/jcc.21334, PMID: 19499576

Ugolev Y, Segal T, Yaffe D, Gros Y, Schuldiner S. 2013. Identification of conformationally sensitive residues essential for inhibition of vesicular monoamine transport by the noncompetitive inhibitor tetrabenazine. *The Journal of Biological Chemistry* **288**:32160–32171. DOI: https://doi.org/10.1074/jbc.M113.502971, PMID: 24062308

Uhlyar S, Rey JA. 2018. Valbenazine (Ingrezza): the first fda-approved treatment for tardive dyskinesia. *P T Peer-Rev. J. Formul. Manag* **43**:328–331.

Vaht M, Kiive E, Veidebaum T, Harro J. 2016. A functional vesicular monoamine transporter 1 (VMAT1) gene variant is associated with affect and the prevalence of anxiety, affective, and alcohol use disorders in a

longitudinal population-representative birth cohort study. *The International Journal of Neuropsychopharmacology* **19**:pyw013. DOI: https://doi.org/10.1093/ijnp/pyw013, PMID: 26861143

Vangone A, Schaarschmidt J, Koukos P, Geng C, Citro N, Trellet ME, Xue LC, Bonvin A. 2019. Large-scale prediction of binding affinity in protein-small ligand complexes: the PRODIGY-LIG web server. *Bioinformatics* **35**:1585–1587. DOI: https://doi.org/10.1093/bioinformatics/bty816, PMID: 31051038

Vanommeslaeghe K, Raman EP, MacKerell AD. 2012. Automation of the CHARMM General Force Field (CGenFF) II: assignment of bonded parameters and partial atomic charges. *Journal of Chemical Information and Modeling* **52**:3155–3168. DOI: https://doi.org/10.1021/ci3003649, PMID: 23145473

Wang YM, Gainetdinov RR, Fumagalli F, Xu F, Jones SR, Bock CB, Miller GW, Wightman RM, Caron MG. 1997. Knockout of the vesicular monoamine transporter 2 gene results in neonatal death and supersensitivity to cocaine and amphetamine. *Neuron* **19**:1285–1296. DOI: https://doi.org/10.1016/s0896-6273(00)80419-5, PMID: 9427251

Wang RY-R, Song Y, Barad BA, Cheng Y, Fraser JS, DiMaio F. 2016. Automated structure refinement of macromolecular assemblies from cryo-EM maps using Rosetta. *eLife* **5**:e17219. DOI: https://doi.org/10.7554/eLife.17219, PMID: 27669148

Weihe E, Schäfer MK, Erickson JD, Eiden LE. 1994. Localization of vesicular monoamine transporter isoforms (VMAT1 and VMAT2) to endocrine cells and neurons in rat. *Journal of Molecular Neuroscience* **5**:149–164. DOI: https://doi.org/10.1007/BF02736730, PMID: 7654518

Wu EL, Cheng X, Jo S, Rui H, Song KC, Dávila-Contreras EM, Qi Y, Lee J, Monje-Galvan V, Venable RM, Klauda JB, Im W. 2014. CHARMM-GUI Membrane Builder toward realistic biological membrane simulations. *Journal of Computational Chemistry* **35**:1997–2004. DOI: https://doi.org/10.1002/jcc.23702, PMID: 25130509

Yaffe D, Radestock S, Shuster Y, Forrest LR, Schuldiner S. 2013. Identification of molecular hinge points mediating alternating access in the vesicular monoamine transporter VMAT2. *PNAS* **110**:E1332–E1341. DOI: https://doi.org/10.1073/pnas.1220497110

Yaffe D, Vergara-Jaque A, Forrest LR, Schuldiner S. 2016. Emulating proton-induced conformational changes in the vesicular monoamine transporter VMAT2 by mutagenesis. *PNAS* **113**:E7390–E7398. DOI: https://doi.org/10.1073/pnas.1605162113

Yaffe D, Forrest LR, Schuldiner S. 2018. The ins and outs of vesicular monoamine transporters. *The Journal of General Physiology* **150**:671–682. DOI: https://doi.org/10.1085/jgp.201711980, PMID: 29666153

Yamashita A, Singh SK, Kawate T, Jin Y, Gouaux E. 2005. Crystal structure of a bacterial homologue of Na+/Cl--dependent neurotransmitter transporters. *Nature* **437**:215–223. DOI: https://doi.org/10.1038/nature03978, PMID: 16041361

Yang D, Gouaux E. 2021. Illumination of serotonin transporter mechanism and role of the allosteric site. *Science Advances* **7**:eabl3857. DOI: https://doi.org/10.1126/sciadv.abl3857, PMID: 34851672

Yao J, Hersh LB. 2007. The vesicular monoamine transporter 2 contains trafficking signals in both its N-glycosylation and C-terminal domains. *Journal of Neurochemistry* **100**:1387–1396. DOI: https://doi.org/10.1111/j.1471-4159.2006.04326.x, PMID: 17217417

Yao Z, Wei X, Wu X, Katz JL, Kopajtic T, Greig NH, Sun H. 2011. Preparation and evaluation of tetrabenazine enantiomers and all eight stereoisomers of dihydrotetrabenazine as VMAT2 inhibitors. *European Journal of Medicinal Chemistry* **46**:1841–1848. DOI: https://doi.org/10.1016/j.ejmech.2011.02.046, PMID: 21396745

Yariv B, Yariv E, Kessel A, Masrati G, Chorin AB, Martz E, Mayrose I, Pupko T, Ben-Tal N. 2023. Using evolutionary data to make sense of macromolecules with a "face-lifted" ConSurf. *Protein Science* **32**:e4582. DOI: https://doi.org/10.1002/pro.4582, PMID: 36718848

Yuan Y, Kong F, Xu H, Zhu A, Yan N, Yan C. 2022. Cryo-EM structure of human glucose transporter GLUT4. *Nature Communications* **13**:2671. DOI: https://doi.org/10.1038/s41467-022-30235-5

Zhang S, Krieger JM, Zhang Y, Kaya C, Kaynak B, Mikulska-Ruminska K, Doruker P, Li H, Bahar I. 2021. ProDy 2.0: increased scale and scope after 10 years of protein dynamics modelling with Python . *Bioinformatics* **37**:3657–3659. DOI: https://doi.org/10.1093/bioinformatics/btab187